Stability and Accuracy of Aeroacoustic Time-Reversal using the Pseudo-Characteristic Formulation

A. Mimani

School of Mechanical Engineering, The University of Adelaide, South Australia 5005, Australia

C. J. Doolan

2 School of Mechanical and Manufacturing Engineering, University of New South Wales, New South Wales 2052, Australia

P. R. Medwell

School of Mechanical Engineering, The University of Adelaide, South Australia 5005, Australia

This paper investigates the stability and accuracy of the aeroacoustic Time-Reversal (TR) simulation using the Pseudo-Characteristic Formulation (PCF). To this end, the forward simulation of acoustic wave propagation in 1-D and 2-D computational domain with a uniform mean flow was implemented using the PCF of the Linearised Euler Equations (LEE). The spatial derivatives in the opposite propagating fluxes of the PCF were computed using an overall upwind-biased Finite-Difference (FD) scheme and a Runge-Kutta scheme was used for time-integration. The anechoic boundary condition (ABC) was implemented for eliminating spurious numerical reflections at the computational boundaries, thereby modelling a free-space. The stability of 1-D forward and TR (with only time-reversed acoustic pressure as the input at the boundary nodes) simulations were analysed by means of an eigenvalue decomposition, wherein it was shown that opposite upwinding directions must be considered while using the overall upwind-biased FD scheme. Furthermore, the implementation of ABC was found to be crucial for ensuring the stability of the forward simulation over a large time duration and the 2-D TR simulations. The overall central Dispersion-Relation Preserving (DRP) FD schemes were however, found to be unstable and unsuitable for TR simulation. The accuracy of both the forward and the TR simulations using the PCF was assessed by comparing the simulation results against the corresponding analytical solutions of a spatially and temporally evolving Gaussian pulse. It was shown that numerically reversing the mean flow direction during TR (using the PCF) and only the time-reversed acoustic pressure as input at the boundaries is sufficient to accurately back-propagate the waves and localise the initial emission point of the pulse in 1-D or 2-D computational domain.

1. INTRODUCTION

The acoustic Time-Reversal (TR) method, developed by Fink, et al.,[1,2] is a promising method to localise acoustic sources in time-domain and is explained by the following two-step procedure:

1. In the first step, the acoustic pressure field radiated by the source(s) is recorded by microphone line arrays (LAs) in a Time-Reversal Mirror (TRM) during experiments, or stored at the boundary nodes (virtual microphones) during forward simulations, either (a) over LAs completely enclosing the sources, or (b) over a limited angular aperture LA(s) that only partially encloses the source(s).

2. In the second step, the recorded acoustic pressure time-history is reversed in time followed by emission from "numerical sources" at the boundary nodes. The back-propagated acoustic pressure signals undergo a constructive interference to form spatio-temporal maxima[3] during TR simulations, which corresponds to the spatial location of the source(s). Method (a) which uses the enclosing LAs, can account for almost the total acoustic power radi-

ated; therefore, back-propagation from this configuration yields the most accurate prediction of the source location, characteristics, and strength. Method (b), however, can account for only a fraction of the acoustic power radiated, thereby limiting the ability of TR to identify the location and nature of sources.[4]

Fink, et al.[2] provide an excellent review of the TR method and discuss its applications in various fields such as hydro-dynamics, ultrasound medical imaging, and diagnostic and non-destructive testing. The TR method has also been used for long-range communication in deep underwater acoustics,[5] structural dynamics for health monitoring,[6] in the presence of a reflecting surface,[7] and in electromagnetic wave propagation.[8] Different methods have been presented to enhance the focal-resolution of TR, namely an active cancellation technique called the Time-Reversal Acoustic Sink (TRAS), developed by Bavu, et al.,[9] and a passive radial damping approach mimicking an acoustic sink called the Point-Time-Reversal-Sponge-Layer (PTRSL), developed by the present authors.[10] The application of the TR method in Computational Aeroacoustics (CAA) for localising sound sources in a flow field is,

however, relatively new. Deneuve, et al.[11] made use of the TR method for the first time to localise aeroacoustics sources. The forward evolution of the pressure and velocity fields was simulated by the numerical solution of the 2-D homoentropic nonlinear Euler equations using the Pseudo-Characteristic Formulation (PCF) proposed by Sesterhenn,[12] wherein the spatial derivatives in the opposite propagating fluxes were computed using an overall upwind-biased Finite-Difference (FD) scheme.[13] As the forward evolution was implemented numerically, it was possible to obtain both the pressure and particle velocity time-histories at the boundary nodes of the rectangular computational domain. Furthermore, the field variables corresponding to the final time instant (during forward simulation) were also stored at all nodes of the domain, and these data were used as an initial condition during the TR simulation. Both the time-reversed pressure and particle velocity, along with the subsonic inflow boundary conditions, were imposed on the computational boundaries during the TR simulation.

The main limitation in the TR simulation (using the PCF[12]) of Deneuve, et al.[11] is the use of time-reversed particle velocity histories at boundary nodes. This is because, in an experimental set-up, only the acoustic pressure may be measured using a microphone LA(s), while it is difficult to simultaneously measure the acoustic particle velocity history. Transducer arrays that can measure both the acoustic pressure and acoustic particle velocities (using 3-D intensity probes) are available with present technology; however, such transducers are usually very expensive. Hence, for practical considerations, measurement of only the acoustic pressure is feasible, and naturally the algorithm implementing the TR simulation using the Linearised Euler Equations[14,15] (LEE) must depend only on the time-reversed acoustic pressure history as the input for accurately localising the acoustic source(s). It is noted that the mean flow profile (about which the Euler equations are linearized) may be measured experimentally using hot-wire anemometry (or other techniques), and that the simulations using the LEE can accurately model the interaction between acoustic perturbations and the mean flow field.[3] Another limitation of the TR simulation of Deneuve, et al.[11] is use of the acoustic pressure and velocity histories stored at all the nodes during the final instant of the forward simulation as the initial condition in the TR simulation. Experimentally measuring and storing the acoustic field over the entire experiment is impossible.

The accuracy, as well as the stability analysis, of TR simulation of the LEE using only the time-reversed acoustic pressure history as the input are, therefore, necessary. Padois, et al.[3] demonstrate the accuracy of TR simulation for localising time-harmonic aeroacoustic sources using only the experimentally obtained acoustic pressure time-history measured over a microphone LA in a TRM located outside of the flow in an Anechoic Wind Tunnel (AWT). Their TR simulations, based on the numerical solution of the 2-D LEE using the 4th order Dispersion Relation Preserving (DRP) central FD schemes,[16] were able to satisfactorily estimate the monopole and dipole source locations in a shear flow field. However, their TR simulation of the LEE was not implemented using the PCF, which splits the derivative of acoustic variables into a pair of opposite propagating fluxes[12] or "pseudo-waves". This feature of the PCF makes it ideally suited for the use of upwind-biased FD schemes in comparison to the Flux-Vector Splitting (FVS) approaches.[17,18] The use of upwind-biased FD schemes is pre-

ferred over the central DRP schemes[16] because the non-zero damping (at the unresolved high-frequencies) in the former is crucial for ensuring the temporal stability of the TR simulation of the LEE, which has not been analysed in the previous works.[3,4,10,11] Indeed, the temporal stability of forward simulation of the LEE based on the PCF and using an overall (a) upwind-biased FD scheme or (b) central DRP FD scheme has also not been analysed previously,[11–13] although the stability of the overall compact FD schemes used for the forward simulation of the simple 1-D scalar wave equation is established.[19] Furthermore, although the aeroacoustic TR simulation is shown to accurately localise sound sources in flow fields,[3,4,10,11] the results have not been compared against the corresponding analytical solution, and hence are not formally validated.

This work, therefore, analyses the temporal stability and accuracy of both the forward and TR simulations of the 1-D and 2-D LEE implemented using the PCF based on (a) an overall upwind-biased FD scheme, and (b) an overall central DRP FD scheme.[16,20] The test cases consist of propagation of an acoustic pulse in both a 1-D and 2-D free-space with mean flow, modelled by the implementation of anechoic boundary condition (ABC) at (1) the terminations of a 1-D duct, and (2) the computational boundaries of a 2-D domain, respectively. The motivation of this analysis is to examine in detail the accuracy of the TR simulation using only the time-reversed acoustic pressure history as the input Dirichlet conditions[3] at the boundaries of the 2-D computational domain (involving the propagation of cylindrical wave fronts). The present work is a part of a larger study that aims to investigate the suitability of TR for experimental aeroacoustics, with a view to obtain important insights into the mechanism of flow-induced turbulent noise generation. Indeed, the authors have implemented TR simulations on experimentally-obtained acoustic pressure data sampled on two LAs of microphones to demonstrate the dipole source nature (at the Aeolian tone) of the flow-induced noise generated by a circular cylinder located in a cross-flow in the AWT of The University of Adelaide.[21] However, the TR is at an early stage in the field of aeroacoustics, and important fundamental work such as that presented here is essential to provide a strong foundation for its future applications.

The paper is organised as follows: Section 2 describes the numerical method for implementing the 1-D/2-D forward and TR simulations of the LEE based on the PCF using the overall upwind-biased FD schemes and implementation of ABC. Section 3 analyses the stability of 1-D forward and TR simulations using the PCF and two classes of overall FD schemes — (a) the upwind-biased FD scheme and (b) the central DRP FD scheme by means of an eigenvalue decomposition. Section 4 analyses the accuracy of 1-D/2-D forward and TR simulation results by comparison against the corresponding analytical solution. The important contributions of this work are then summarised in Section 5.

2. METHODOLOGY: NUMERICAL IMPLEMENTATION OF THE SIMULATIONS

In this section, the numerical implementation of the forward and TR simulations on 1-D and 2-D computational domains (in Cartesian coordinates) is described. To this end, the homogenous 2-D LEE of continuity and momentum (assuming
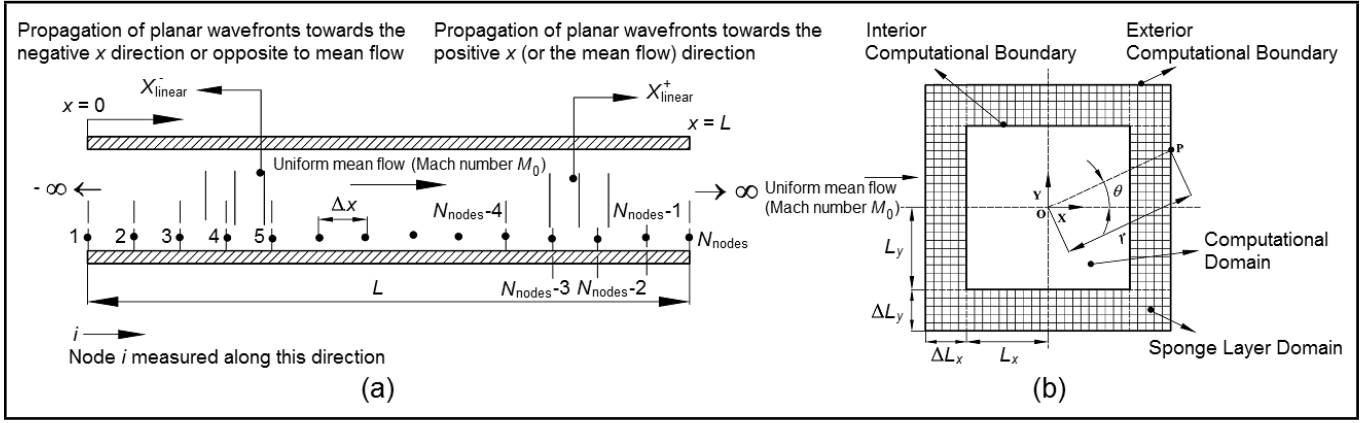
Figure 1. (a) A schematic illustrating the discretisation of a 1-D duct of finite length L (modelling a 1-D free-space) into finite parts (Δx), convention to number the nodes and fluxes ($X_{\text{linear}}^{\pm}$ propagating towards the positive and negative x directions, respectively). (b) A 2-D computational domain fully surrounded by a sponge-layer domain modelling a 2-D free space. The half-length of the computational domain and width of the sponge-layer domain are L_x and ΔL_x along the x direction, respectively, L_y and ΔL_y along the y direction, respectively. The direction of uniform mean flow is considered towards the positive x direction in parts (a) and (b).

homoentropic flow) are considered, and are shown below.[14, 15]

$$\frac{\partial \tilde{\rho}}{\partial t} + U_0 \frac{\partial \tilde{\rho}}{\partial x} + \rho_0 \left(\frac{\partial \tilde{u}}{\partial x} + \frac{\partial \tilde{v}}{\partial y} \right) = 0; \qquad (1a)$$

$$\rho_0 \frac{\partial \tilde{u}}{\partial t} + \rho_0 U_0 \frac{\partial \tilde{u}}{\partial x} + \frac{\partial \tilde{p}}{\partial x} = 0; \qquad (1b)$$

$$\rho_0 \frac{\partial \tilde{v}}{\partial t} + \rho_0 U_0 \frac{\partial \tilde{v}}{\partial x} + \frac{\partial \tilde{p}}{\partial y} = 0; \qquad (1c)$$

where $\{\tilde{p}(x, y, t), \tilde{\rho}(x, y, t), \tilde{u}(x, y, t), \tilde{v}(x, y, t)\}$ are the acoustic pressure (Pa), acoustic density (kgm^{-3}), and acoustic particle velocities (ms^{-1}) along the x and y direction, respectively, U_0 is the subsonic uniform mean flow velocity (ms^{-1}) towards the positive x direction, ρ_0 is the ambient density, taken as 1.21 kgm^{-3}, and t is the forward time (s). Furthermore, isentropic conditions are assumed, so that $c_0^2 = \tilde{p}/\tilde{\rho}$, where c_0 denotes the uniform sound speed, taken as 343.14 ms^{-1} in this work. The 1-D homogenous LEE may be obtained by neglecting the spatial variation along the y direction, i.e. ignoring Eq. (1c) and dropping the $(\partial \tilde{v}/\partial y)$ term from Eq. (1a).

2.1. Forward Simulation

2.1.1. Pseudo-Characteristic Formulation (PCF) of the Linearised Euler Equations (LEE)

The forward simulations are implemented by first recasting the homogenous 2-D LEE shown in Eqs. (1a–c) in the PCF[11–13] as

$$\frac{\partial \tilde{p}}{\partial t} = -\frac{\rho_0 c_0}{2} \left(X_{\text{linear}}^+ + X_{\text{linear}}^- + Y_{\text{linear}}^+ + Y_{\text{linear}}^- \right); \qquad (2a)$$

$$\frac{\partial \tilde{u}}{\partial t} = -\frac{1}{2} \left(X_{\text{linear}}^+ - X_{\text{linear}}^- \right); \qquad (2b)$$

$$\frac{\partial \tilde{v}}{\partial t} = -\frac{1}{2} \left(Y_{\text{linear}}^+ - Y_{\text{linear}}^- \right) - c_0 M_0 \frac{\partial \tilde{v}}{\partial x}; \qquad (2c)$$

where

$$X_{\text{linear}}^{\pm} = \pm c_0 (1 \pm M_0) \left\{ \frac{1}{\rho_0 c_0} \frac{\partial \tilde{p}}{\partial x} \pm \frac{\partial \tilde{u}}{\partial x} \right\}; \qquad (3)$$

$$Y_{\text{linear}}^{\pm} = \pm c_0 \left\{ \frac{1}{\rho_0 c_0} \frac{\partial \tilde{p}}{\partial y} \pm \frac{\partial \tilde{v}}{\partial y} \right\}; \qquad (4)$$

and $M_0 = U_0/c_0$ is the Mach number of subsonic uniform mean flow. In Eqs. (2–4), X_{linear}^+ denotes the acoustic flux propagating towards the positive x direction with an enhanced speed of $c_0(1 + M_0)$, while X_{linear}^- denotes the acoustic flux propagating towards the negative x direction with a reduced speed of $c_0(1 - M_0)$, respectively. Similarly, $Y_{\text{linear}}^{\pm}$ denotes fluxes propagating with a speed c_0 towards the positive and negative y directions, respectively. It is noted that the splitting of the LEE into a pair of opposing fluxes ($X_{\text{linear}}^{\pm}, Y_{\text{linear}}^{\pm}$) facilitate a straightforward implementation of the upwind-biased FD schemes and anechoic boundary condition (ABC),[11, 13] which is necessary for suppressing the unresolved spurious high frequency waves, thereby stabilising the simulations. Furthermore, the $c_0 M_0 (\partial \tilde{v}/\partial x)$ term in Eq. (2c) denotes acoustic disturbances advected by the mean flow towards the positive x direction.[13]

2.1.2. Spatial and Temporal Discretization

An overall upwind-biased FD scheme is formulated for computing the spatial derivatives of the acoustic pressure and velocities in the opposing fluxes ($X_{\text{linear}}^{\pm}, Y_{\text{linear}}^{\pm}$) in Eqs. (2a–c). To this end, a 1-D computational domain along the x direction of a finite length L modelled by a duct (with only planar wave propagation) is considered in Fig. 1(a). This domain is discretized into N_{nodes} number of equally spaced nodes of mesh size $\Delta x = L/(N_{\text{nodes}} - 1)$.

The spatial derivative $(\partial \phi/\partial x)^+$ of the acoustic field variable ϕ ($\tilde{p}$, $\tilde{u}$ or $\tilde{v}$) in the X_{linear}^+ flux for the entire 1-D domain is computed using the overall upwind-biased FD schemes formulated in Table 1. It is noted that the use of optimised downwind FD schemes[20, 22] at the penultimate and last nodes of the boundaries, as well as the use of 3$^{\text{rd}}$ and 5$^{\text{th}}$ order upwind-biased schemes[23] near the boundary nodes, is necessary because sufficient upwind nodes do not exist near the boundary for use of the 7-point, 4$^{\text{th}}$ order optimised upwind-biased DRP FD scheme.[22]

The overall upwind-biased FD schemes used for computing the spatial derivative $(\partial \phi/\partial x)^-$ in the X_{linear}^- flux for the entire 1-D domain is similarly formulated by making use of opposite upwinding directions at a node i (with the sign of the stencil coefficients reversed). The efficiency of implementing the overall upwind-biased FD schemes is increased by recasting

Table 1. Overall upwind-biased FD Scheme for computing $(\partial\phi/\partial x)^+$ in the flux X_{linear}^+

Nodes	FD Scheme and formal order of accuracy	Stencil Coefficients
$i = N_{\text{nodes}}$	$\frac{1}{\Delta x}\sum_{k=0}^{k=6} b_{-k}^{60}\phi(N_{\text{nodes}} - k),$ 4th order (Tam[20])	$\begin{cases} b_0^{60} = 2.1922803, & b_{-1}^{60} = -4.7486114, & b_{-2}^{60} = 5.1088519, \\ b_{-3}^{60} = -4.4615671, & b_{-4}^{60} = 2.8334987, & b_{-5}^{60} = -1.1283289, \\ b_{-6}^{60} = 0.2038764. & & \end{cases}$
$i = N_{\text{nodes}}-1$	$\frac{1}{\Delta x}\sum_{k=-5}^{k=1} a_k^{51}\phi(i+k),$ 4th order (Zhuang and Chen[22])	$\begin{cases} a_{-5}^{51} = -0.0306490, & a_{-4}^{51} = 0.2022259, & a_{-3}^{51} = -0.6347280, \\ a_{-2}^{51} = 1.2962997, & a_{-1}^{51} = -2.1430548, & a_0^{51} = 1.1088873, \\ a_1^{51} = 0.2010190. & & \end{cases}$
$5 \le i \le N_{\text{nodes}}-2$	$\frac{1}{\Delta x}\sum_{k=-4}^{k=2} a_k^{42}\phi(N_{\text{nodes}} - 1 + k),$ 4th order (Zhuang and Chen[22])	$\begin{cases} a_{-4}^{42} = 0.0161405, & a_{-3}^{42} = -0.1228213, & a_{-2}^{42} = 0.4553323, \\ a_{-1}^{42} = -1.2492596, & a_0^{42} = 0.5018904, & a_1^{42} = 0.4399322, \\ a_2^{42} = -0.0412145. & & \end{cases}$
$i = 4$	$\frac{1}{\Delta x}\sum_{k=-3}^{k=2} a_k^{32}\phi(4+k),$ 5th order (Li[23])	$\begin{cases} a_{-3}^{32} = -1/30, & a_{-2}^{32} = 1/4, & a_{-1}^{32} = -1, \\ a_0^{32} = 1/3, & a_1^{32} = 1/2, & a_2^{32} = -1/20. \end{cases}$
$i = 3$	$\frac{1}{\Delta x}\sum_{k=-2}^{k=1} a_k^{21}\phi(3+k),$ 3rd order (Li[23])	$\begin{cases} a_{-2}^{21} = 1/6, & a_{-1}^{21} = -1, & a_0^{21} = 1/2, & a_1^{21} = 1/3. \end{cases}$
$i = 2$	$\frac{1}{\Delta x}\sum_{k=-1}^{k=5} a_k^{15}\phi(2+k),$ 4th order (Zhuang and Chen[22])	$\begin{cases} a_{-1}^{15} = -a_1^{51}, & a_0^{15} = -a_0^{51}, & a_1^{15} = -a_{-1}^{51}, & a_2^{15} = -a_{-2}^{51} \\ a_3^{15} = -a_{-3}^{51}, & a_4^{15} = -a_{-4}^{51}, & a_5^{15} = -a_{-5}^{51}. & \end{cases}$
$i = 1$	$\frac{1}{\Delta x}\sum_{k=0}^{k=6} b_k^{06}\phi(1+k),$ 4th order (Tam[20])	$\begin{cases} b_0^{06} = -b_0^{60}, & b_1^{06} = -b_{-1}^{60}, & b_2^{06} = -b_{-2}^{60}, & b_3^{06} = -b_{-3}^{60} \\ b_4^{06} = -b_{-4}^{60}, & b_5^{06} = -b_{-5}^{60}, & b_6^{06} = -b_{-6}^{60}. & \end{cases}$

them in the following matrix form:

$$\frac{\partial\{\phi\}^+}{\partial x} \approx \frac{1}{\Delta x}[\mathbf{R_1}]\{\phi\}; \qquad (5a)$$

$$\frac{\partial\{\phi\}^-}{\partial x} \approx \frac{1}{\Delta x}[\mathbf{R_2}]\{\phi\}; \qquad (5b)$$

where $\{\phi\} = \{\phi_1, \phi_2, \phi_3, \ldots, \phi_{N_{\text{nodes}}}\}^T$. The spatial derivatives in the fluxes $Y_{\text{linear}}^{\pm}$ are also computed using Eqs. (5a, b) while the $(\partial\tilde{v}/\partial x)$ term in Eq. (2c) is computed using Eq. (5a), as the mean flow direction is towards the positive x direction. The use of two different stencil groups at a given node (or opposite upwinding directions) ensures that the inbuilt dissipation in upwind-biased schemes damps only the unresolved high-frequency waves and does not induce spatially growing oscillations with time, which is important for temporal stability. This is explained by the following discussion:

A harmonic wave $\tilde{p}(x, t = 0) = e^{jk_0 x}$ is considered as an initial disturbance where $j = \sqrt{-1}$ and k_0 is the exact wavenumber. The numerical solution of the wave propagating towards positive x direction is given by[24]

$$\tilde{p}(x,t) = e^{j(k_0 x - \tilde{\omega}t)} = e^{j(k_0 x - \tilde{k}c_0 t)} =$$
$$\underbrace{e^{j[k_0 - \text{Re}(\tilde{k})]c_0 t}}_{\text{dispersion}} \cdot \underbrace{e^{\text{Im}(\tilde{k})c_0 t}}_{\text{dissipation}} \cdot \underbrace{e^{jk_0(x - c_0 t)}}_{\text{exact solution}}; \qquad (6)$$

where $\tilde{\omega}$ is the numerical angular frequency and $\tilde{k} = \tilde{\omega}/c_o$ is the numerical wavenumber given by $\beta = k_0\Delta x \approx \tilde{k}\Delta x = -j\left\{\sum_{k=-N}^{k=M} a_k^{NM} e^{j(k\beta)}\right\}$, in which β is the exact non-dimensional wave number and a_k^{NM} are stencil coefficients of a $N + M + 1$ point FD stencil. Equation (6) indicates that for non-dispersive and non-dissipative frequency region given by $\{k_0 - \text{Re}(\tilde{k})\} \to 0$ and $\text{Im}(\tilde{k}) \to 0$, respectively, the numerical solution is an accurate approximation to the exact solution. However, for the unresolved or dispersive frequency region,

i.e. $\{k_0 - \text{Re}(\tilde{k})\} \neq 0$, the dissipation should be such that $\text{Im}(\tilde{k}) < 0$ to ensure temporal stability of the numerical solution of the wave propagating towards the positive x direction. Similarly, for temporal stability of the numerical solution of the wave propagating towards the negative x direction, the dissipation should be such that $\text{Im}(\tilde{k}) > 0$ in dispersive frequency region.

The 3rd order Total-Variation-Diminishing (TVD) Runge-Kutta scheme[25] is used for time-integration during the 1-D and 2-D forward simulations, as well as for TR simulations. The time-step Δt is computed a-priori forward simulations in accordance with the Courant–Friedrichs–Lewy (CFL) number equal to 0.2 considered to ensure accuracy of the forward/TR simulations. Equal mesh size given by $\Delta x = \Delta y = 0.005$ m is taken along the x and y directions, respectively, in the 2-D simulations. Furthermore, the same mesh size, $\Delta x = 0.005$ m, is also considered during the 1-D simulations. It is noted that amongst all the FD schemes used to formulate the overall upwind-biased FD scheme (in Table 1), the 4-point, 3rd order standard upwind-biased FD scheme[23] has the least DRP range given by $\alpha_{\text{DRP}} = \tilde{k}_{\text{max}}\Delta x \approx 0.62$, and determines the maximum wavenumber $\tilde{k}_{\text{max}}$ that can be accurately propagated (i.e. without significant dispersion). For the mesh sizes (Δx, Δy) and c_0, the maximum wavenumber resolution band evaluates to $\tilde{k}_{\text{max}} = [0, \alpha_{\text{DRP}}/\Delta x] = [0, 124]$ m^{-1}.

2.1.3. Implementation of the Anechoic Boundary Condition (ABC)

The ABCs are implemented at the computational boundaries to model a 1-D free-space (represented by a 1-D duct extending infinitely on both sides, as shown in Fig. 1(a)) and a 2-D free-space shown in Fig. 1(b). For the case of 1-D free-space, the ABC is implemented by setting the incoming fluxes to zero at the finite terminations of the duct,[11, 13] i.e. $X_{\text{linear}}^+|_{x=0} = 0$ and $X_{\text{linear}}^-|_{x=L} = 0$, which implies that the

impedance $\tilde{p}_{i-1}/(-\tilde{u}_{i-1}) = \tilde{p}_{i=N_{\text{nodes}}}/\tilde{u}_{i=N_{\text{nodes}}} = \rho_0 c_0$, i.e. the characteristic impedance of the medium. Hence, the acoustic wave impinging on the boundaries is completely transmitted without suffering any reflection. The use of $X_{\text{linear}}^+\big|_{x=0} = 0$ and $X_{\text{linear}}^-\big|_{x=L} = 0$ boundary conditions is equivalent to the first order Clayton-Engquist-Majda (CEM) ABCs given by[26–28]

$$\left(\frac{\partial \tilde{p}}{\partial t} - c_0 (1 - M_0) \frac{\partial \tilde{p}}{\partial x}\right)\bigg|_{x=0} = 0; \quad \text{and} \quad (7)$$

$$\left(\frac{\partial \tilde{p}}{\partial t} + c_0 (1 + M_0) \frac{\partial \tilde{p}}{\partial x}\right)\bigg|_{x=L} = 0; \quad (8)$$

respectively, which is exact for the 1-D acoustic wave propagation in a mean flow.

The 2-D computational domain given by $|x| \leq L_x, |y| \leq L_y$ fully surrounded by a sponge-layer domain of widths ΔL_x and ΔL_y along the x and y directions, respectively, as shown in Fig. 1(b) models a 2-D free-space. At the exterior computational boundary, the first-order radiation boundary condition of Tam and Webb[16] (henceforth, referred to as Tam's ABC) is used. The Tam's ABC condition reads

$$\frac{1}{V(\theta)}\frac{\partial \tilde{p}}{\partial t} + \frac{\partial \tilde{p}}{\partial r} + \frac{\tilde{p}}{2r} = 0 \quad \Rightarrow$$
$$\frac{1}{V(\theta)}\frac{\partial \tilde{p}}{\partial t} + \cos\theta\frac{\partial \tilde{p}}{\partial x} + \sin\theta\frac{\partial \tilde{p}}{\partial y} + \frac{\tilde{p}}{2\sqrt{x^2+y^2}} = 0; \quad (9)$$

where $r = (x^2 + y^2)^{1/2}$ is the radius of the point $\mathbf{P}$ on the exterior computational boundary from the initial position of the peak of Gaussian pulse (i.e. the known source location) denoted by origin $\mathbf{O}$, θ is the angle with respect to the x axis, and $V(\theta) = c_0 \left(M_0 \cos\theta + (1 - M_0^2 \sin^2\theta)^{1/2}\right)$ is the convective sound speed (due to subsonic mean flow M_0), considering the directional dependence. It is noted that since the acoustic field at the exterior computational boundary comprises only the outgoing waves, the spatial derivatives $(\partial \tilde{p}/\partial x, \partial \tilde{p}/\partial y)$ in Eq. (9) are computed in accordance with the value of θ at a particular node. This is discussed as follows:

1. $0 \leq \theta \leq \pi/2$, $\partial \tilde{p}/\partial x$ and $\partial \tilde{p}/\partial y$ are both computed using Eq. (5a);

2. $\pi/2 < \theta \leq \pi$, $\partial \tilde{p}/\partial y$ and $\partial \tilde{p}/\partial x$ are computed using Eq. (5a) and Eq. (5b), respectively;

3. $\pi < \theta \leq 3\pi/2$, $\partial \tilde{p}/\partial x$ and $\partial \tilde{p}/\partial y$ are both computed using Eq. (5b); and

4. $3\pi/2 \leq \theta < 2\pi$, $\partial \tilde{p}/\partial y$ and $\partial \tilde{p}/\partial x$ are computed using Eq. (5b) and Eq. (5a), respectively.

In order to further suppress the spurious reflections during the 2-D forward simulations, the incoming fluxes near the exterior computational boundary are damped over several nodes (N_{sponge}) of a sponge-layer domain[13] with a width of $\Delta L_x = N_{\text{sponge}}\Delta x$ and $\Delta L_y = N_{\text{sponge}}\Delta y$ along the x and y directions, respectively, fully surrounding the computational domain. The damping is implemented using the following equa-

tions:

$$Y_{\text{linear}}^{\mp}(x, \pm L_y \pm (N_{\text{sponge}} - n)\Delta y) \rightarrow \quad (10a)$$
$$Y_{\text{linear}}^{\mp}(x, \pm L_y \pm (N_{\text{sponge}} - n)\Delta y) \times G_{\text{sponge}}(n); \quad (10b)$$
$$X_{\text{linear}}^{\mp}(\pm L_x \pm (N_{\text{sponge}} - n)\Delta x, y) \rightarrow \quad (10c)$$
$$X_{\text{linear}}^{\mp}(\pm L_x \pm (N_{\text{sponge}} - n)\Delta x, y) \times G_{\text{sponge}}(n); \quad (10d)$$

where

$G_{\text{sponge}}(n = 0) = 0$ and $G_{\text{sponge}}(n) = e^{-\frac{1}{2}\left(\alpha_{\text{sponge}}\left(\frac{N_{\text{sponge}} - n}{N_{\text{sponge}} - 1}\right)\right)^2}$ for $n = [1, 2, \ldots, N_{\text{sponge}} - 1]$. Here, α_{sponge} is the damping coefficient taken equal to four in this work. It is noted that implementation of Tam's ABC (with or without the inclusion of sponge-layer domain) at boundaries of the 2-D computational domain is crucial for the temporal stability of forward simulation of a pulse propagating in a free-space over a large time duration. The condition $(\partial \tilde{v}/\partial x)\big|_{x=-L_x-\Delta L_x} = 0$ is also implemented to suppress the incoming waves at the $x = -L_x - \Delta L_x$ boundary advected by the mean flow, thereby preventing instability.

2.2. Time-Reversal (TR) Simulation

The 2-D forward simulations are implemented over a sufficiently large time-interval $t = [0, T]$ such that the pulse completely propagates out of the domain, whereby the acoustic pressure $\tilde{p}(x, y, t)$ and particle velocities $\tilde{u}(x, y, t)$, $\tilde{v}(x, y, t)$ are stored at the nodes of all four computational boundaries, i.e. at $x = \pm L_x, |y| \leq L_y$ and $y = \pm L_y, |x| \leq L_x$ after every time-step. The 2-D TR simulation is implemented by first introducing the following transformations[3,4,10,11] in Eqs. (2–4):

$$t \rightarrow T - \tilde{t}; \quad (11a)$$
$$\tilde{p}(x, y, t) \rightarrow \tilde{p}(x, y, \tilde{t}); \quad (11b)$$
$$\tilde{u}(x, y, t) \rightarrow -\tilde{u}(x, y, \tilde{t}); \quad (11c)$$
$$\tilde{v}(x, y, t) \rightarrow -\tilde{v}(x, y, \tilde{t}); \quad (11d)$$

to obtain the time-reversed 2-D LEE (in the PCF) shown as follows:[10,11]

$$\frac{\partial \tilde{p}}{\partial \tilde{t}} = -\frac{\rho_0 c_0}{2}\left\{\tilde{X}_{\text{linear}}^+ + \tilde{X}_{\text{linear}}^- + \tilde{Y}_{\text{linear}}^+ + \tilde{Y}_{\text{linear}}^-\right\}; \quad (12a)$$

$$\frac{\partial \tilde{u}}{\partial \tilde{t}} = -\frac{1}{2}\left(\tilde{X}_{\text{linear}}^+ - \tilde{X}_{\text{linear}}^-\right); \quad (12b)$$

$$\frac{\partial \tilde{v}}{\partial \tilde{t}} = -\frac{1}{2}\left(\tilde{Y}_{\text{linear}}^+ - \tilde{Y}_{\text{linear}}^-\right) - c_0(-M_0)\frac{\partial \tilde{v}}{\partial x}; \quad (12c)$$

where

$$\tilde{X}_{\text{linear}}^{\pm} = \pm c_0(1 \mp M_0)\left\{\frac{1}{\rho_0 c_0}\frac{\partial \tilde{p}}{\partial x} \pm \frac{\partial \tilde{u}}{\partial x}\right\}; \quad (13a)$$

$$\tilde{Y}_{\text{linear}}^{\pm} = \pm c_0\left\{\frac{1}{\rho_0 c_0}\frac{\partial \tilde{p}}{\partial y} \pm \frac{\partial \tilde{v}}{\partial y}\right\}; \quad (13b)$$

and $\tilde{t}$ denotes the reverse time. It is noted that the time-reversed 2-D LEE given by Eqs. (12a–c) are identical to Eqs. (2a–c), except that the direction of subsonic mean flow is reversed in $\tilde{X}_{\text{linear}}^{\pm}$ fluxes and in the $(\partial \tilde{v}/\partial x)$ term. The reversal of mean flow direction $(M_0 \rightarrow -M_0)$ during the numerical TR simulation (and not in the physical sense) is essential to ensure TR invariance.[3,4,10,11] Furthermore, the derivative $(\partial \tilde{v}/\partial x)$ in

Eq. (12c) is computed using Eq. (5b) due to reversal of the mean flow.

The 2-D TR simulation is implemented using either (a) only $\tilde{p}(x,y,\tilde{t})$, or (b) both $\tilde{p}(x,y,\tilde{t})$ and $-\tilde{u}(x,y,\tilde{t})$, $-\tilde{v}(x,y,\tilde{t})$ as input Dirichlet boundary conditions[3] (which enables the back-propagation of waves into the domain) at $x = \pm L_x$ and $y = \pm L_y$ boundaries after every reverse time-step. It is noted that the sponge-layer domain is not used during the 2-D TR simulation; rather, it is found that implementation of the CEM ABC[26–28] at all four boundaries given by

$$\left(\frac{\partial \tilde{p}}{\partial \tilde{t}} \pm c_0(1 \mp M_0)\frac{\partial \tilde{p}}{\partial x} \right)\bigg|_{x=\pm L_x} = 0; \qquad (14a,b)$$

$$\left(\frac{\partial \tilde{p}}{\partial \tilde{t}} \pm c_0\frac{\partial \tilde{p}}{\partial y} \right)\bigg|_{y=\pm L_y} = 0; \qquad (14c,d)$$

and at the four corners of the 2-D domain, the use of special corner ABC[28] given by

$$\frac{\partial \tilde{p}}{\partial \tilde{t}} + \frac{c_0}{\sqrt{2}}(1-M_0)\frac{\partial \tilde{p}}{\partial x} + \frac{c_0}{\sqrt{2}}\frac{\partial \tilde{p}}{\partial y}\bigg|_{x=L_x,y=L_y} = 0; \quad (15a)$$

$$\frac{\partial \tilde{p}}{\partial \tilde{t}} - \frac{c_0}{\sqrt{2}}(1+M_0)\frac{\partial \tilde{p}}{\partial x} + \frac{c_0}{\sqrt{2}}\frac{\partial \tilde{p}}{\partial y}\bigg|_{x=-L_x,y=L_y} = 0; \quad (15b)$$

$$\frac{\partial \tilde{p}}{\partial \tilde{t}} - \frac{c_0}{\sqrt{2}}(1+M_0)\frac{\partial \tilde{p}}{\partial x} - \frac{c_0}{\sqrt{2}}\frac{\partial \tilde{p}}{\partial y}\bigg|_{x=-L_x,y=-L_y} = 0; \quad (15c)$$

$$\frac{\partial \tilde{p}}{\partial \tilde{t}} + \frac{c_0}{\sqrt{2}}(1-M_0)\frac{\partial \tilde{p}}{\partial x} - \frac{c_0}{\sqrt{2}}\frac{\partial \tilde{p}}{\partial y}\bigg|_{x=L_x,y=-L_y} = 0; \quad (15d)$$

is necessary for the temporal stability of 2-D TR simulations.[4,10] In comparison to Tam's ABC, the CEM ABC and the special corner ABC are relatively less accurate in modelling non-reflective boundaries. Nonetheless, it is implemented at the computational boundaries because unlike the forward simulation, the radial distance r of a boundary node from the source location during TR simulation is not known; rather, the robustness of TR algorithm (in a 2-D free-space) must be demonstrated through accurate localization of the source(s) with implementation of approximate ABCs that does not depend on an a-priori estimate of the source location. It is noted that in Eqs. (14a), (15a), and (15d), the spatial derivative $\partial \tilde{p}/\partial x$ at nodes on the $x = L_x$ boundary is computed using Eq. (5a), while $\partial \tilde{p}/\partial x$ at nodes on the $x = -L_x$ boundary in Eqs. (14b), (15b), and (15c) is computed using Eq. (5b). Furthermore, in Eqs. (14c), (15a), and (15b), the spatial derivative $\partial \tilde{p}/\partial y$ at nodes on the $y = L_y$ boundary is computed using Eq. (5a), while $\partial \tilde{p}/\partial y$ at nodes on the $y = -L_y$ boundary in Eqs. (14d), (15c), and (15d) is computed using Eq. (5b). In addition, the incoming normal acoustic fluxes (of the PCF[12] of the 2-D LEE) are also set to zero at the computational boundaries, i.e. $\tilde{X}_{\text{linear}}^{\pm}\big|_{x=\mp L_x} = \tilde{Y}_{\text{linear}}^{\pm}\big|_{y=\mp L_y} = 0$ to reinforce the ABCs during TR simulation.[4,10] The boundary condition $(\partial \tilde{v}/\partial x)\big|_{x=L_x} = 0$ is implemented for the stability of 2-D TR simulation. The 1-D TR simulation is implemented by ignoring Eq. (12c) and the $\tilde{Y}_{\text{linear}}^{\pm}$ fluxes in Eq. (12a) and solving the resultant time-reversed 1-D LEE (in the PCF) with only the time-reversed acoustic pressure as the input Dirichlet condition at the boundary nodes. However, it is found that the use of ABC at the boundary nodes is not necessary for stability of 1-D TR simulation.

3. STABILITY ANALYSIS OF THE 1-D FORWARD AND TR SIMULATIONS: EIGENVALUE DECOMPOSITION

The temporal stability of the forward and TR simulations in the 1-D infinite duct with mean flow using the overall upwind-biased FD scheme and the PCF is evaluated using eigenvalue decomposition. The objective of this analysis is to establish the stability associated with the implementation of the correct upwinding directions in the antagonistic fluxes of the PCF and the appropriate boundary conditions using a 1-D test case.

3.1. Forward Simulation

An eigenvalue problem for an acoustic pulse propagating in the 1-D duct with a mean flow is formulated. To this end, the $[\mathbf{R_1}]$ and $[\mathbf{R_2}]$ matrices are used for computing the spatial derivatives of $\{\tilde{p}\}$ and $\{\tilde{u}\}$ in the $\tilde{X}_{\text{linear}}^{\pm}$ fluxes, respectively, in the PCF of the 1-D LEE. Rearranging the resultant equations in terms of the linear combination of $\{\tilde{p}\}$ and $\{\rho_0 c_0 \tilde{u}\}$ yields the following set of semi-discretised ordinary differential equations:

$$\frac{d\{\tilde{p}\}}{dt} = -\frac{c_0}{2(\Delta x)}\bigg\{ \Big[(1+M_0)[\mathbf{R_1}] + (M_0-1)[\mathbf{R_2}] \Big]\{\tilde{p}\}$$
$$+ \Big[(1+M_0)[\mathbf{R_1}] - (M_0-1)[\mathbf{R_2}] \Big]\{\rho_0 c_0 \tilde{u}\} \bigg\}; \quad (16a)$$

$$\frac{d\{\rho_0 c_0 \tilde{u}\}}{dt} = -\frac{c_0}{2(\Delta x)}\bigg\{ \Big[(1+M_0)[\mathbf{R_1}] + (1-M_0)[\mathbf{R_2}] \Big]\{\tilde{p}\}$$
$$+ \Big[(1+M_0)[\mathbf{R_1}] - (1-M_0)[\mathbf{R_2}] \Big]\{\rho_0 c_0 \tilde{u}\} \bigg\}. \quad (16b)$$

By substituting $\{\tilde{p}\} = \{\hat{p}\}e^{\omega t}$ and $\{\rho_0 c_0 \tilde{u}\} = \{\rho_0 c_0 \hat{u}\}e^{\omega t}$ in Eqs. (16a, b) and subsequent algebraic manipulations, the following eigenvalue problem is obtained:

$$[\mathbf{A}]\Big\{ \{\hat{p}\}_{N_{\text{nodes}}} \quad \{\rho_0 c_0 \hat{u}\}_{N_{\text{nodes}}} \Big\}^T = \lambda \Big\{ \{\hat{p}\}_{N_{\text{nodes}}} \quad \{\rho_0 c_0 \hat{u}\}_{N_{\text{nodes}}} \Big\}^T; \quad (17a)$$

where ω represents the dimensional eigenvalues (complex, in general), $\{\hat{p}\}$ and $\{\rho_0 c_0 \hat{u}\}$ denote the corresponding eigenvectors, the matrix $[\mathbf{A}]$ is given by

$$[\mathbf{A}]_{2N_{\text{nodes}} \times 2N_{\text{nodes}}} = -\frac{1}{2} \times$$
$$\begin{bmatrix} (1+M_0)[\mathbf{R_1}]+(M_0-1)[\mathbf{R_2}] & (1+M_0)[\mathbf{R_1}]-(M_0-1)[\mathbf{R_2}] \\ (1+M_0)[\mathbf{R_1}]+(1-M_0)[\mathbf{R_2}] & (1+M_0)[\mathbf{R_1}]-(1-M_0)[\mathbf{R_2}] \end{bmatrix}; \quad (17b)$$

and $\lambda = (\omega \Delta x)/c_0$ denotes the corresponding non-dimensional eigenvalues of the $[\mathbf{A}]$ matrix. The solution of Eqs. (16a, b) is now obtained in terms of the matrix exponential as[29]

$$\Big\{ \tilde{p}(t) \quad \rho_0 c_0 \tilde{u}(t) \Big\}^T = e^{[\mathbf{A}]\frac{c_0 t}{\Delta x}}\Big\{ \tilde{p}(t=0) \quad \rho_0 c_0 \tilde{u}(t=0) \Big\}^T; \quad (17c)$$

whereby it becomes evident that the stability of the overall FD scheme depends on the whether the $\text{Re}(\lambda)$ is positive or negative. It is noted that Eqs. (16a, b) are cast in a semi-discrete form because only the spatial derivatives of the acoustic variables are approximated by overall FD schemes, and

time-integration is not considered at this stage. Thus, by assuming modes of the form $\{\tilde{\phi}\} = \{\hat{\phi}\}e^{\omega t}$, discretisation errors due to numerical time-integration are avoided. Therefore, in the eigenvalue problem for the forward simulation given by Eqs. (17a, b), a perfect time-integration is considered[19] and the stability of only spatial discretisation is analysed. Similar conclusions also hold for the eigenvalue analysis of the 1-D TR simulation. Furthermore, it is noted that no boundary conditions are specified in Eq. (17a). However, in order to analyse the temporal stability of the forward simulation of a pulse propagating in the 1-D infinite duct, it is necessary to implement the ABCs by setting $X_{\text{linear}}^{+}\big|_{x=0} = 0$ and $X_{\text{linear}}^{-}\big|_{x=L} = 0$ in Eqs. (17a, b), thereby leading to

$$[\mathbf{A}_{\text{anechoic}}]\Big\{\{\hat{p}\}_{N_{\text{nodes}}} \quad \{\rho_0 c_0 \hat{u}\}_{N_{\text{nodes}}}\Big\}^{T} =$$
$$\lambda\Big\{\{\hat{p}\}_{N_{\text{nodes}}} \quad \{\rho_0 c_0 \hat{u}\}_{N_{\text{nodes}}}\Big\}^{T}; \quad (18)$$

where $[\mathbf{A}_{\text{anechoic}}]$ is defined by Eq. (19), which is the eigenvalue problem incorporating the ABC at both boundaries of the finite 1-D duct.

Figure 2(a) presents the eigenvalue loci of the eigenvalue problem posed in Eq. (18) using the overall upwind-biased FD schemes for $X_{\text{linear}}^{\pm}$ fluxes that are used to simulate the test case 1 with $N_{\text{nodes}} = 1500$ for $M_0 = 0$ and $M_0 = 0.30$. It is evident from Fig. 2(a) that the eigenvalue loci of Eq. (18) consists of closed loop(s) located on the negative side of the real-axis ($\text{Re}(\lambda)$ axis), indicating that opposite upwinding directions in the $X_{\text{linear}}^{\pm}$ fluxes of the PCF (by means of $[\mathbf{R_1}]$ and $[\mathbf{R_2}]$ matrices, respectively) are necessary for temporal stability. Furthermore, the implementation of the ABC at the first and last node of the computational domain (unlike Lu and Sagaut,[13] wherein the ABC was implemented at the first and the last five nodes of the 2-D domain) entirely shifts the eigenvalue loci to the negative side of the $\text{Re}(\lambda)$ axis. Indeed, none of the eigenvalues have positive real parts (regardless of their magnitude), and in order to justify this claim, an exaggerated view of the eigenvalue loci near the imaginary axis in Fig. 2(b) is presented. The lone eigenvalue in each of the loci shown in Fig. 2(b) located 'almost' at the origin has a negative real part of the order of 10^{-7}, thereby implying rather slow decay, but most importantly, a stable solution. Therefore, the implementation of ABC prevents the occurrence of eigenvalues with small positive real parts (of the order of 10^{-3}), which are liable to induce instabilities over large duration (or at later instants) of the forward simulation.[30]

The effect of a subsonic mean flow on the eigenvalue locus of the overall upwind-biased FD scheme is also illustrated in Fig. 2, wherein the mean flow is shown to 'bifurcate' the locus horizontally so that there exists two different loci on the negative side of the $\text{Re}(\lambda)$ axis of the λ plane. One of the eigenvalue locus corresponding to the wave propagation 'along' the direction of superimposed mean flow is shifted farther towards the negative side of the $\text{Re}(\lambda)$ axis, thereby implying an enhanced stability, whereas the eigenvalue locus corresponding to the wave propagation 'against' the direction of mean flow is shifted towards the imaginary-axis ($\text{Im}(\lambda)$ axis). However, for subsonic mean flow, this locus is still entirely situated on the negative side of the $\text{Re}(\lambda)$ axis, thereby allaying any concerns on the stability issue. These two loci converge or coalesce into a single locus that is oriented vertically near the $\text{Im}(\lambda)$ axis.

The effect of the number of nodes N_{nodes} on the eigenvalue locus of the overall upwind-biased FD scheme was also studied for the case of zero mean flow (results not shown here). It was observed that with an increase in N_{nodes} the eigenvalue envelope expands further towards the negative side of the real axis, thereby indicating enhanced stability. However, these envelopes do not converge; rather, they expand monotonically as N_{nodes} is increased, thereby indicating that there does not exist a set of discrete natural frequencies for a finite length duct with ABC on both the sides which essentially models a system extending infinitely in both the directions.[31]

Another stability analysis (shown in Fig. 3) was performed for $M_0 = 0$ using an overall central FD scheme formulated as: (1) the 7-point, 4th order accurate central DRP FD scheme of Tam,[16] which are used at the interior nodes $4 \leq i \leq N_{\text{nodes}} - 3$, and (2) the 7-point optimised backward or downwind FD schemes,[20] which are used at the nodes $i = 1, 2, 3$ and $i = N_{\text{nodes}} - 2, N_{\text{nodes}} - 1, N_{\text{nodes}}$. (In this case, $[\mathbf{R_1}] = [\mathbf{R_2}] = [\mathbf{R_0}]$, thus the spatial derivatives in $\tilde{X}_{\text{linear}}^{\pm}$ is computed using the $[\mathbf{R_0}]$ matrix.)

It is observed from Fig. 3, that this overall central DRP FD schemes encounter a mild instability problem associated with the implementation of ABC at the first and last node only. This is because instability starts creeping into the solution (due to the eventual growth in the exponential solution due to very small real parts of the eigenvalues) after the pulse has completely propagated outside the domain. To circumvent this problem, the ABC was implemented at two or more nodes on each side of the boundary, wherein it is observed that in the last three cases presented in Fig. 3, the eigenvalue loci increasingly shifts entirely towards the negative side of the $\text{Re}(\lambda)$ axis of the λ plane, thereby stabilising the 1-D forward simulation using the overall central DRP FD scheme.

3.2. TR Simulation

The temporal stability of the 1-D TR simulation is investigated by first deriving the semi-discretised form of the 1-D LEE for implementing the TR simulation. To this end, the mean flow direction is reversed ($M_0 \rightarrow -M_0$) in Eqs. (16a, b), whereby the following matrix form is obtained:

$$\frac{d}{d\tilde{t}}\left\{\begin{array}{c}\{\tilde{p}\} \\ \{\rho_0 c_0 \tilde{u}\}\end{array}\right\} = \frac{c_0}{\Delta x}[\mathbf{A_0}]\left\{\begin{array}{c}\{\tilde{p}\} \\ \{\rho_0 c_0 \tilde{u}\}\end{array}\right\}; \quad (20a)$$

where

$$[\mathbf{A_0}]_{2N_{\text{nodes}} \times 2N_{\text{nodes}}} = -\frac{1}{2} \times$$
$$\begin{bmatrix} (1-M_0)[\mathbf{R_1}]-(1+M_0)[\mathbf{R_2}] & (1-M_0)[\mathbf{R_1}]+(1+M_0)[\mathbf{R_2}] \\ (1-M_0)[\mathbf{R_1}]+(1+M_0)[\mathbf{R_2}] & (1-M_0)[\mathbf{R_1}]-(1+M_0)[\mathbf{R_2}] \end{bmatrix};$$
$$(20b)$$

Equation (20a) presents the homogeneous ordinary differential matrix form of the time-reversed 1-D LEE for the temporal solution of the spatially discretized acoustic pressure and velocity fields. (The forward time t in Eqs. (16a, b) is simply replaced with the reverse time $\tilde{t}$ in Eq. (20a).) The time-history of the acoustic pressure $\tilde{p}(i = 1, \tilde{t})$ and $\tilde{p}(i = N_{\text{nodes}}, \tilde{t})$ at the boundary nodes are, however, known a-priori for $\tilde{t} = [0, T]$ at discrete time-instants from the 1-D forward simulations.

$[\mathbf{A}_{\text{anechoic}}]_{2N_{\text{nodes}} \times 2N_{\text{nodes}}} =$

$$
-\frac{1}{2}
\left[
\begin{array}{c|c}
(M_0 - 1) \left[R_2^{1,1} \quad \ldots \quad R_2^{1,N_{\text{nodes}}} \right]_{1 \times N_{\text{nodes}}} & (1 - M_0) \left[R_2^{1,1} \quad \ldots \quad R_2^{1,N_{\text{nodes}}} \right]_{1 \times N_{\text{nodes}}} \\[2mm]
\left[\begin{array}{ccc} A^{2,1} & \ldots & A^{2,N_{\text{nodes}}} \\ \vdots & \ddots & \vdots \\ A^{N_{\text{nodes}}-1,1} & \ldots & A^{N_{\text{nodes}}-1,N_{\text{nodes}}} \end{array} \right]_{(N_{\text{nodes}}-2) \times N_{\text{nodes}}} & \left[\begin{array}{ccc} A^{2,N_{\text{nodes}}+1} & \ldots & A^{2,2N_{\text{nodes}}} \\ \vdots & \ddots & \vdots \\ A^{N_{\text{nodes}}-1,N_{\text{nodes}}+1} & \ldots & A^{N_{\text{nodes}}-1,2N_{\text{nodes}}} \end{array} \right]_{(N_{\text{nodes}}-2) \times N_{\text{nodes}}} \\[2mm]
(1 + M_0) \left[R_1^{N_{\text{nodes}},1} \quad \ldots \quad R_1^{N_{\text{nodes}},N_{\text{nodes}}} \right]_{1 \times N_{\text{nodes}}} & (1 + M_0) \left[R_1^{N_{\text{nodes}},1} \quad \ldots \quad R_1^{N_{\text{nodes}},N_{\text{nodes}}} \right]_{1 \times N_{\text{nodes}}} \\[2mm]
\hline
(1 - M_0) \left[R_2^{1,1} \quad \ldots \quad R_2^{1,N_{\text{nodes}}} \right]_{1 \times N_{\text{nodes}}} & (M_0 - 1) \left[R_2^{1,1} \quad \ldots \quad R_2^{1,N_{\text{nodes}}} \right]_{1 \times N_{\text{nodes}}} \\[2mm]
\left[\begin{array}{ccc} A^{N_{\text{nodes}}+2,1} & \ldots & A^{N_{\text{nodes}}+2,N_{\text{nodes}}} \\ \vdots & \ddots & \vdots \\ A^{2N_{\text{nodes}}-1,1} & \ldots & A^{2N_{\text{nodes}}-1,N_{\text{nodes}}} \end{array} \right]_{(N_{\text{nodes}}-2) \times N_{\text{nodes}}} & \left[\begin{array}{ccc} A^{N_{\text{nodes}}+2,N_{\text{nodes}}+1} & \ldots & A^{N_{\text{nodes}}+2,2N_{\text{nodes}}} \\ \vdots & \ddots & \vdots \\ A^{2N_{\text{nodes}}-1,N_{\text{nodes}}+1} & \ldots & A^{2N_{\text{nodes}}-1,2N_{\text{nodes}}} \end{array} \right]_{(N_{\text{nodes}}-2) \times N_{\text{nodes}}} \\[2mm]
(1 + M_0) \left[R_1^{N_{\text{nodes}},1} \quad \ldots \quad R_1^{N_{\text{nodes}},N_{\text{nodes}}} \right]_{1 \times N_{\text{nodes}}} & (1 + M_0) \left[R_1^{N_{\text{nodes}},1} \quad \ldots \quad R_1^{N_{\text{nodes}},N_{\text{nodes}}} \right]_{1 \times N_{\text{nodes}}}
\end{array}
\right] ;
$$

$$(19)$$

Therefore, for the analysis of the temporal stability of TR simulations, the rows $i = 1$ and $i = N_{\text{nodes}}$ of the $[\mathbf{A_0}]$ matrix (corresponding to the semi-discretised continuity equation at boundary nodes) are discarded, while the corresponding columns $i = 1$ and $i = N_{\text{nodes}}$ are rearranged in the $[\mathbf{B}_{\text{TR}}]$ matrix shown as follows:

$$
\frac{d\{\mathbf{\Psi}\}}{d\tilde{t}} = \frac{c_0}{\Delta x}[\mathbf{A}_{\text{TR}}]\{\mathbf{\Psi}\} + \frac{c_0}{\Delta x}[\mathbf{B}_{\text{TR}}] \left\{ \begin{array}{c} \tilde{p}_1 \\ \tilde{p}_{N_{\text{nodes}}} \end{array} \right\}_{2 \times 1} ; \quad (21a)
$$

where

$$
\{\mathbf{\Psi}\}_{(2N_{\text{nodes}}-2) \times 1} =
$$

$$
\left\{ \tilde{p}_2(\tilde{t}) \ldots \tilde{p}_{N_{\text{nodes}}-1}(\tilde{t}) \quad \rho_0 c_0 \tilde{u}_1(\tilde{t}) \ldots \rho_0 c_0 \tilde{u}_{N_{\text{nodes}}}(\tilde{t}) \right\}^T ; \quad (21b)
$$

$[\mathbf{A}_{\text{TR}}]$ is given by Eq. (21c), and

$$
[\mathbf{B}_{\text{TR}}]_{(2N_{\text{nodes}}-2) \times 2} = \left[\begin{array}{cc} A_0^{2,1} & A_0^{2,N_{\text{nodes}}} \\ \vdots & \vdots \\ A_0^{N_{\text{nodes}}-1,1} & A_0^{N_{\text{nodes}}-1,N_{\text{nodes}}} \\ A_0^{N_{\text{nodes}}+1,1} & A_0^{N_{\text{nodes}}+1,N_{\text{nodes}}} \\ \vdots & \vdots \\ A_0^{2N_{\text{nodes}},1} & A_0^{2N_{\text{nodes}},N_{\text{nodes}}} \end{array} \right] . \quad (21d)
$$

It is noted that Eq. (21a) is an inhomogeneous matrix differential equation. The inhomogeneity in Eq. (21a) is ascribed to the presence of the non-zero acoustic pressure vector $\{\tilde{p}_1 \ \tilde{p}_{N_{\text{nodes}}}\}^T$. This vector acts as a numerical source during each time-step of TR simulations and initiates and sustains a back-propagation of acoustic pulses in the computational domain during $\tilde{t} = [0, T]$ which eventually coalesces at $\tilde{t} = T$. It is also noted that solving the time-reversed 1-D LEE in the inhomogeneous form is equivalent to the numerical time-integration of Eq. (20a) immediately followed by the enforcement of time-reversed acoustic pressure $\tilde{p}(i = 1, \tilde{t})$ and $\tilde{p}(i = N_{\text{nodes}}, \tilde{t})$ at the boundary nodes. The stability of implementation of the 1-D TR simulation using the PCF and the overall upwind-biased FD scheme can now be assessed using

the exact temporal solution of Eq. (21a) expressed as

$$
\left\{ \tilde{p}_2 \ldots \tilde{p}_{N_{\text{nodes}}-1} \quad \rho_0 c_0 \tilde{u}_1 \ldots \rho_0 c_0 \tilde{u}_{N_{\text{nodes}}} \right\}^T =
$$

$$
\frac{c_0}{\Delta x} e^{[\mathbf{A}_{\text{TR}}]\frac{c_0 \tilde{t}}{\Delta x}} \left\{ \int_{\tau=0}^{\tau=\tilde{t}} e^{-[\mathbf{A}_{\text{TR}}]\frac{c_0 \tau}{\Delta x}} [\mathbf{B}_{\text{TR}}] \left\{ \begin{array}{c} \tilde{p}_1(\tau) \\ \tilde{p}_{N_{\text{nodes}}}(\tau) \end{array} \right\} d\tau \right\} .
$$

$$(22)$$

Equation (22) is a formal representation of the exact temporal solution; however, the TR simulation is not implemented using this formal solution. This is because the exact function expressing the variation of the vector $\{\tilde{p}_1(\tau) \ \tilde{p}_{N_{\text{nodes}}}(\tau)\}^T$ with time τ is not known a-priori, rather $\tilde{p}(i = 1, \tilde{t})$ and $\tilde{p}(i = N_{\text{nodes}}, \tilde{t})$ time-histories are known at only discrete values of $\tilde{t}$. Nonetheless, Eq. (22) can be used for a stability analysis of the TR method by examining the eigenvalues of the $[\mathbf{A}_{\text{TR}}]$ matrix. The TR simulations are stable if all the eigenvalues of the $[\mathbf{A}_{\text{TR}}]$ matrix have negative or zero real parts (provided that the parameters of the $[\mathbf{B}_{\text{TR}}]$ matrix and the inhomogeneous vector $\{\tilde{p}_1(\tau) \ \tilde{p}_{N_{\text{nodes}}}(\tau)\}^T$ are finite). It is for this reason that the inhomogeneous part of Eq. (21a) is disregarded in formulating the eigenvalue problem. On substituting $\{\mathbf{\Psi}\}^T = \{\hat{\mathbf{\Psi}}\}^T e^{\omega \tilde{t}}$ in Eq. (21a) and subsequent algebraic manipulations, the following eigenvalue problem is posed:

$$
[\mathbf{A}_{\text{TR}}]\{\hat{\mathbf{\Psi}}\}^T = \lambda\{\hat{\mathbf{\Psi}}\}^T; \quad (23a)
$$

$$
\{\hat{\mathbf{\Psi}}\}^T = \left\{ \tilde{p}_2 \ldots \tilde{p}_{N_{\text{nodes}}-1} \quad \rho_0 c_0 \tilde{u}_1 \ldots \rho_0 c_0 \tilde{u}_{N_{\text{nodes}}} \right\}^T; \quad (23b)
$$

where λ denotes the non-dimensional eigenvalues of the $[\mathbf{A}_{\text{TR}}]$ matrix.

Figure 4 presents the eigenvalue loci of the $[\mathbf{A}_{\text{TR}}]$ matrix for $N_{\text{nodes}} = 1500$. It is observed from Fig. 4(a) that the eigenvalue loci for $M_0 = 0$ and $M_0 = 0.30$ consists of a closed loop mostly located on the negative side of the $\text{Re}(\lambda)$ axis, thereby demonstrating the stability and robustness of the 1-D TR simulations by considering two different upwinding directions (to compute the spatial derivatives in opposing fluxes $\tilde{X}_{\text{linear}}^{\pm}$) while using the overall upwind-biased FD schemes formulated here. Figure 4(b) depicts an exaggerated view of the
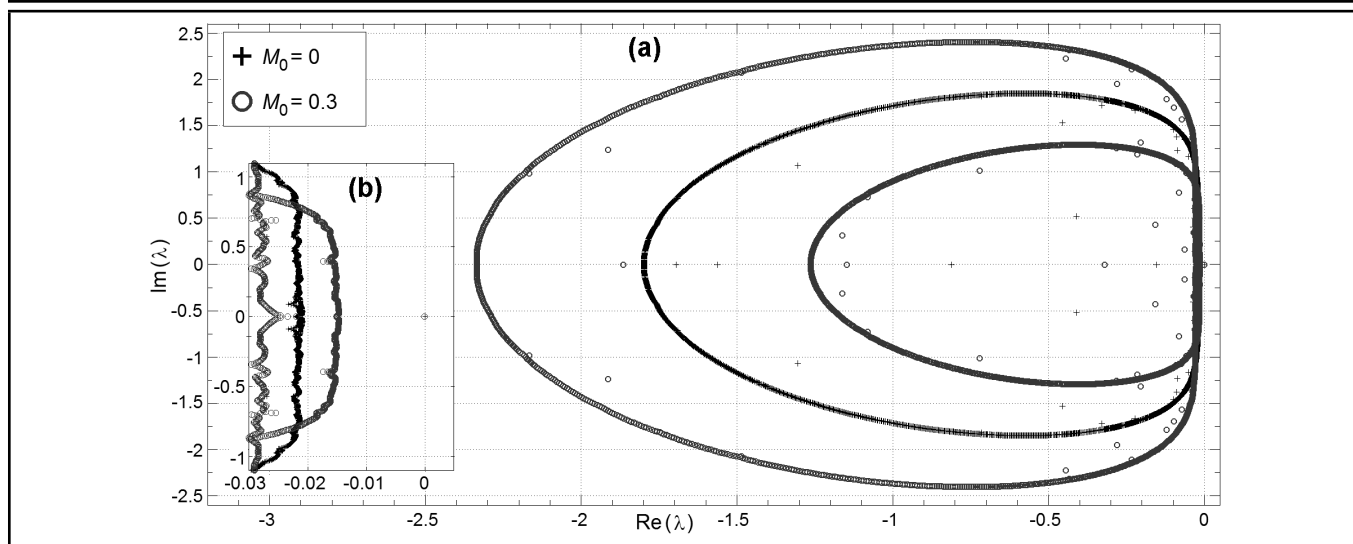
Figure 2. Eigenvalue loci of the overall upwind-biased FD scheme obtained from Eq. (18): Illustration of the stability with implementation of the ABC and the bifurcating effect of a mean flow.
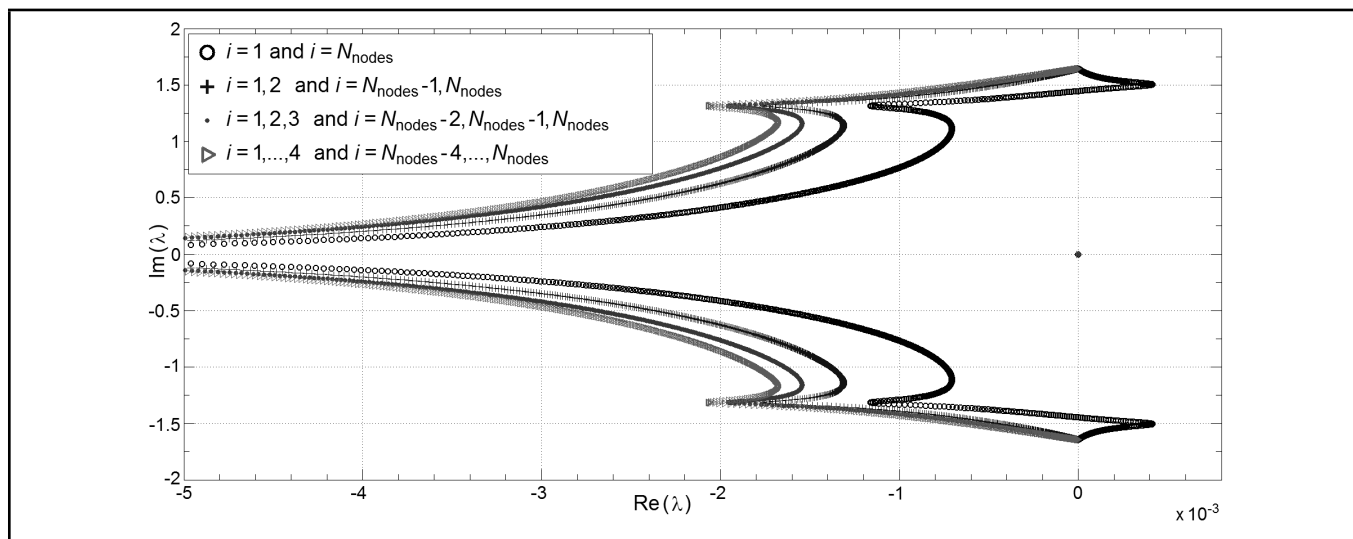

Figure 3. Stabilising effect of enforcing ABC on the first two (or more) and the last two (or more) nodes of the computational domain on the eigenvalue loci of the overall central DRP FD scheme.

eigenvalue loci near the imaginary axis. It is observed that the enlarged eigenvalue loci for $M_0 = 0$ and $M_0 = 0.30$ have very small positive real parts whose magnitudes are of the order of 10^{-5} or even smaller. This suggests a mild instability problem in the strict sense, which might be a concern only over a large duration of TR simulation. Indeed, it is observed that these mild instabilities do not affect the accuracy and robustness of TR (shown in subsections 4.1.2 and 4.2.2) in predicting the initial location of the pulse.

The eigenvalue loci of the $[\mathbf{A}_{\mathrm{TR}}]$ matrix using the overall central DRP FD schemes[16,20] are presented in Fig. 5(a) for $N_{\mathrm{nodes}} = 1500$. Two different mean flow values given by $M_0 = 0$ and $M_0 = 0.30$ are also considered for evaluating the stability of overall central DRP FD schemes.[16,20]

It is observed from Figs. 5(a, b) that for both the stationary medium as well as for the moving medium, the eigenvalue loci resemble a straight line aligned vertically along the imaginary axis. Some of the eigenvalues have large positive real parts (of the order of 10^{-1}) which signify the rapid growth of instabilities during the TR simulations. An enlarged view of the eigenvalue loci is depicted in Fig. 5(b), wherein it is ob-

served that the eigenvalues are clustered along the imaginary axis. The magnitudes of the real part of these eigenvalues are of the order 10^{-4} (an order of magnitude greater than the unstable eigenvalues shown in Fig. 4(b)). Therefore, based on these features of the eigenvalue loci shown in Fig. 5, it may be concluded that the overall central FD schemes have eigenvalues with relatively larger positive real parts, and thus are more prone to instabilities. To conclude, the overall central DRP FD scheme (without the Artificial Selective Damping[32] (ASD)) is thus unsuitable for simulation of Euler equations for TR application. It may however be mentioned that inclusion of the extraneous ASD terms in the LEE while using the overall central DRP FD scheme stabilizes the 1-D TR simulation. This is because the eigenvalue loci would shift entirely to the negative side of the $\mathrm{Re}(\lambda)$ axis of the λ plane (so that none of the eigenvalues have a positive real part), and its shape would resemble the eigenvalue loci of the overall upwind-biased FD scheme shown in Fig. 4. Indeed, similar conclusions also hold for the effect of ASD on the 1-D forward simulation using the overall central DRP FD scheme. It is important to note that the damping in the ASD stencil is directly proportional to the in-

$$[\mathbf{A}_{\mathrm{TR}}]_{(2N_{\mathrm{nodes}}-2)\times(2N_{\mathrm{nodes}}-2)} =$$

$$
\begin{bmatrix}
\begin{bmatrix} A_0^{2,2} & \cdots & A_0^{2,N_{\mathrm{nodes}}-1} \\ \vdots & \ddots & \vdots \\ A_0^{N_{\mathrm{nodes}}-1,2} & \cdots & A_0^{N_{\mathrm{nodes}}-1,N_{\mathrm{nodes}}-1} \end{bmatrix}_{(N_{\mathrm{nodes}}-2)\times(N_{\mathrm{nodes}}-2)} & \begin{bmatrix} A_0^{2,N_{\mathrm{nodes}}+1} & \cdots & A_0^{2,2N_{\mathrm{nodes}}} \\ \vdots & \ddots & \vdots \\ A_0^{N_{\mathrm{nodes}}-1,N_{\mathrm{nodes}}+1} & \cdots & A_0^{N_{\mathrm{nodes}}-1,2N_{\mathrm{nodes}}} \end{bmatrix}_{(N_{\mathrm{nodes}}-2)\times N_{\mathrm{nodes}}} \\[2em]
\begin{bmatrix} A_0^{N_{\mathrm{nodes}}+1,2} & \cdots & A_0^{N_{\mathrm{nodes}}+1,N_{\mathrm{nodes}}-1} \\ \vdots & \ddots & \vdots \\ A_0^{2N_{\mathrm{nodes}},2} & \cdots & A_0^{2N_{\mathrm{nodes}},N_{\mathrm{nodes}}-1} \end{bmatrix}_{N_{\mathrm{nodes}}\times(N_{\mathrm{nodes}}-2)} & \begin{bmatrix} A_0^{N_{\mathrm{nodes}}+1,N_{\mathrm{nodes}}+1} & \cdots & A_0^{N_{\mathrm{nodes}}+1,2N_{\mathrm{nodes}}} \\ \vdots & \ddots & \vdots \\ A_0^{2N_{\mathrm{nodes}},N_{\mathrm{nodes}}+1} & \cdots & A_0^{2N_{\mathrm{nodes}},2N_{\mathrm{nodes}}} \end{bmatrix}_{N_{\mathrm{nodes}}\times N_{\mathrm{nodes}}}
\end{bmatrix};
$$

(21c)

verse mesh Reynolds number (R_Δ^{-1}), and therefore in practice, R_Δ^{-1} is chosen in a rather ad-hoc manner (and is specific to a particular CAA problem) such that the ASD does not induce any inaccuracy due to over-damping.[32] It is noted that the foregoing remarks on the stability of 1-D simulations also hold for overall upwind-biased or central FD schemes formulated using other available FD schemes such as the wavenumber extended schemes of Li,[23] optimised scheme of Lockard,[33] and the 15-point central DRP FD scheme of Tam.[34]

4. RESULTS AND DISCUSSION: ACCURACY ANALYSIS OF THE SIMULATIONS

The accuracy of the 1-D and 2-D forward simulation and the TR simulation (implemented using only the time-reversed acoustic pressure as input at the boundary nodes) is analysed by comparison with the corresponding analytical solution of the acoustic pressure field due to the propagation of an acoustic pulse in a mean flow field involving planar wave fronts in the 1-D duct and cylindrical wave fronts in the 2-D free-space.

4.1. Test Case 1: Propagation of a Gaussian Pulse in an Infinite 1-D Duct with Mean Flow

The initial acoustic pressure field $\phi(x)$ is taken as a Gaussian function. Therefore, $\tilde{p}(x, t=0) = \phi(x) = \varepsilon e^{-\alpha(x-x_0)^2}$ where ε is the initial amplitude of the pulse, x_0 denotes the initial location of the peak of the Gaussian pulse in the 1-D domain given by $0 \le x \le 1$, and α pertains to the sharpness of the pulse and decides the maximum wavenumber content computed by the Fourier transform $\frac{1}{\sqrt{2\pi}} \int_{x=-\infty}^{x=\infty} e^{-\alpha x^2} e^{-jk_0 x} dx = \left(e^{-\frac{k_0^2}{4\alpha}}/\sqrt{2\alpha} \right)$. In the ensuing simulation results, $\varepsilon = 0.1$ Pa and $\alpha = 100$ m^{-2}, and therefore the maximum wavenumber content k_0 of the 1-D Gaussian pulse is less than 40 m^{-1}, thereby indicating that the spatial discretisation and the overall upwind-biased FD scheme warrants an accurate acoustic wave propagation. Furthermore, $x_0 = 0.5$ m and $M_0 = 0.3$ are considered; hence, $\Delta t_1 = 2.2418 \times 10^{-6}$ s based on the CFL number equal to 0.2.

4.1.1. Forward Simulation

Figures 6(a–d) compare the spatio-temporal evolution of the acoustic pressure field predicted by the 1-D forward simulation against the corresponding analytical solution of the prop-

agation of a Gaussian pulse in an infinite 1-D duct with mean flow (given by Eq. (24)) at time-instants (a) $t = 0$ (Initial condition), (b) $t = 200\Delta t_1$, (c) $t = 400\Delta t_1$, and (d) $t = 700\Delta t_1$, respectively.

$$\tilde{p}_{\mathrm{analytical}}(x, t) = \frac{1}{2} \times$$
$$\left\{ \overbrace{\underbrace{\phi(x - (1 + M_0)c_0 t)}_{}}^{\text{Pulse propagating along the positive } x \text{ direction}} + \underbrace{\phi(x + (1 + M_0)c_0 t)}_{\text{Pulse propagating along the negative } x \text{ direction}} \right\}. \quad (24)$$

An excellent agreement is observed from Fig. 6(a–d) between the forward simulation and the analytical solution at all time-instants, thereby establishing the accuracy of 1-D forward simulations. It is observed that the initial Gaussian pulse starts decaying and splitting into two Gaussian pulses of equal amplitude but propagating in opposite directions with unequal speeds (due to convective effect of mean flow). The pulse propagating towards the positive x direction propagates at an enhanced speed $c_0(1 + M_0) = 1.3c_0$ and leaves the domain earlier than the pulse that propagates towards negative x direction at the reduced speed $c_0(1 - M_0) = 0.7c_0$.

The forward simulations were carried out for a large time-interval $t = [0, T_1 = 3000\Delta t_1]$ during which the pulse completely propagates out of the domain and the acoustic pressure and particle velocities are vanishingly small (less than machine precision) beyond this interval.

In order to formally assess the accuracy, a L_1 norm error between the $\tilde{p}(x, t)$ and $\rho_0 c_0 \tilde{u}(x, t)$ fields predicted by the forward simulations and the corresponding 1-D analytical solutions is defined as

$$L_1^p(t) = \frac{1}{L} \int_{x=0}^{x=L=1} |\tilde{p}_{\mathrm{analytical}}(x, t) - \tilde{p}(x, t)| \, dx; \quad (25a)$$

$$L_1^u(t) = \frac{1}{L} \int_{x=0}^{x=L=1} \rho_0 c_0 |\tilde{u}_{\mathrm{analytical}}(x, \tilde{t}) - \tilde{u}(x, t)| \, dx; \quad (25b)$$

and has been evaluated at every time-step of the forward simulations. It is observed from Fig. 7(a) that for the initial time duration of forward simulation $t = [0, 1500\Delta t]$, the $L_1^p(t)$ and $L_1^u(t)$ norm errors are equal and of the order 10^{-7} for the overall upwind-biased scheme, whereas the $\tilde{p}(x, t)$ and $\rho_0 c_0 \tilde{u}(x, t)$ fields are of the order 10^{-2} (maximum value over the domain $0 \le x \le 1$) during this interval, thereby formally validating the 1-D forward simulation using the PCF and overall upwind-biased FD schemes.
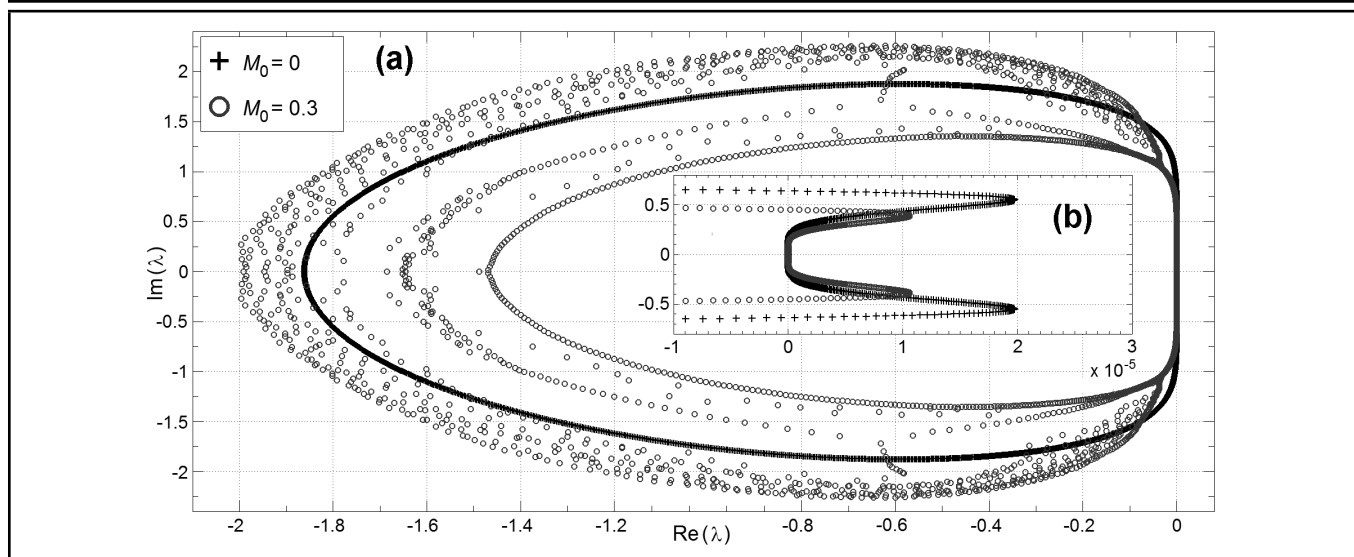
Figure 4. Eigenvalue loci of the $[\mathbf{A}_{\mathrm{TR}}]$ matrix shown in Eq. (21c) for $N_{\mathrm{nodes}} = 1500$ based on the overall upwind-biased FD scheme: Illustration of stability and the bifurcating effect of a mean flow M_0.
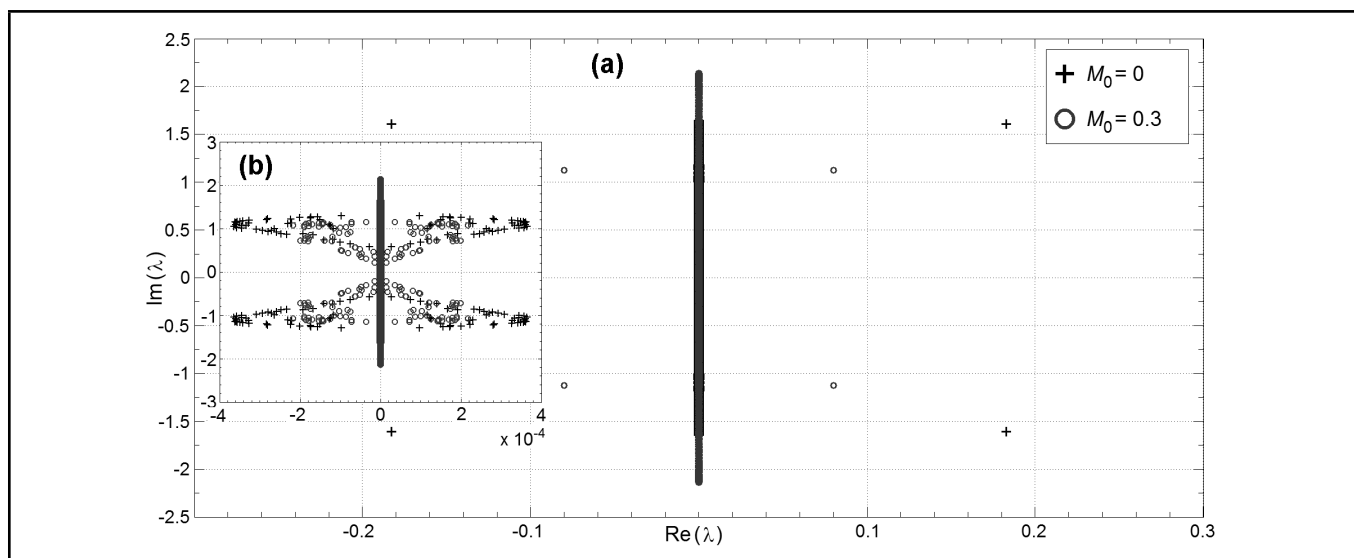

Figure 5. Eigenvalue loci of the $[\mathbf{A}_{\mathrm{TR}}]$ matrix shown in Eq. (21c) for $N_{\mathrm{nodes}} = 1500$ based on the overall central DRP FD schemes: Illustration of instability during the TR simulation due to a few eigenvalues with large positive real parts.

The 1-D forward simulations were also implemented using the overall central DRP FD schemes[16, 20] (discussed in Section 3) wherein a numerically stable and accurate solution was obtained. Indeed, the $L_1^p(t)$ and $L_1^u(t)$ norm errors in this case were almost identical to that of the overall upwind-biased FD schemes due to the similar resolution characteristics (DRP property) of the 4th order, the 7-point central DRP FD stencil[16] and the 4th order, and the 7-point optimised upwind-biased FD stencil.[22] However, it was observed that the relative execution time of the forward simulations per time-step using the overall central DRP FD scheme is approximately half that taken by the overall upwind-biased FD schemes.

4.1.2. TR Simulation

Figures 6(d–a) show the $\tilde{p}(x, \tilde{t})$ field predicted by the 1-D TR simulation using only the time-reversed acoustic pressure as input at the boundary nodes ($i = 1, N_{\mathrm{nodes}}$) at discrete time-instants (d) $\tilde{t} = 2300\Delta t_1$, (c) $\tilde{t} = 2600\Delta t_1$, (b) $\tilde{t} = 2800\Delta t_1$, and (a) $\tilde{t} = T_1 = 3000\Delta t_1$ (the final time-instant of the TR simulation), respectively. It is noted that during the 1-D TR

simulation, the ABCs have not been implemented at the finite termination of the duct. The $\tilde{p}(x, \tilde{t})$ field obtained by the 1-D TR simulation is found to be in excellent agreement with the $\tilde{p}(x, t)$ field predicted by the forward simulation, and also with the time-reversed analytical solution (obtained by replacing t with $T - \tilde{t}$ in Eq. (24)) at the corresponding time-instants. It is observed that two Gaussian pulses of equal amplitude back propagate into the computational domain at unequal speeds (the pulse propagating from the $x = 0$ and the $x = L$ boundary propagate at a speed of $0.7c_0$ and $1.3c_0$, respectively), undergo constructive interference, and eventually coalesce at $\tilde{t} = T_1$ to form a single amplified Gaussian pulse at the same spatial location ($x = x_0$) and amplitude as the initial Gaussian pulse (at $t = 0$ during the forward simulation), thereby revealing the correct source location and amplitude. For formally assessing the accuracy, a L_1 norm error between the $\tilde{p}(x, \tilde{t})$ and $\rho_0 c_0 \tilde{u}(x, \tilde{t})$ fields predicted by the 1-D TR simulation and the corresponding time-reversed analytical solutions has also been evaluated at every time-step of the TR simulation. The $L_1^p(\tilde{t})$ and $L_1^u(\tilde{t})$ versus $\tilde{t}$ graphs are presented in Fig. 7(b). It
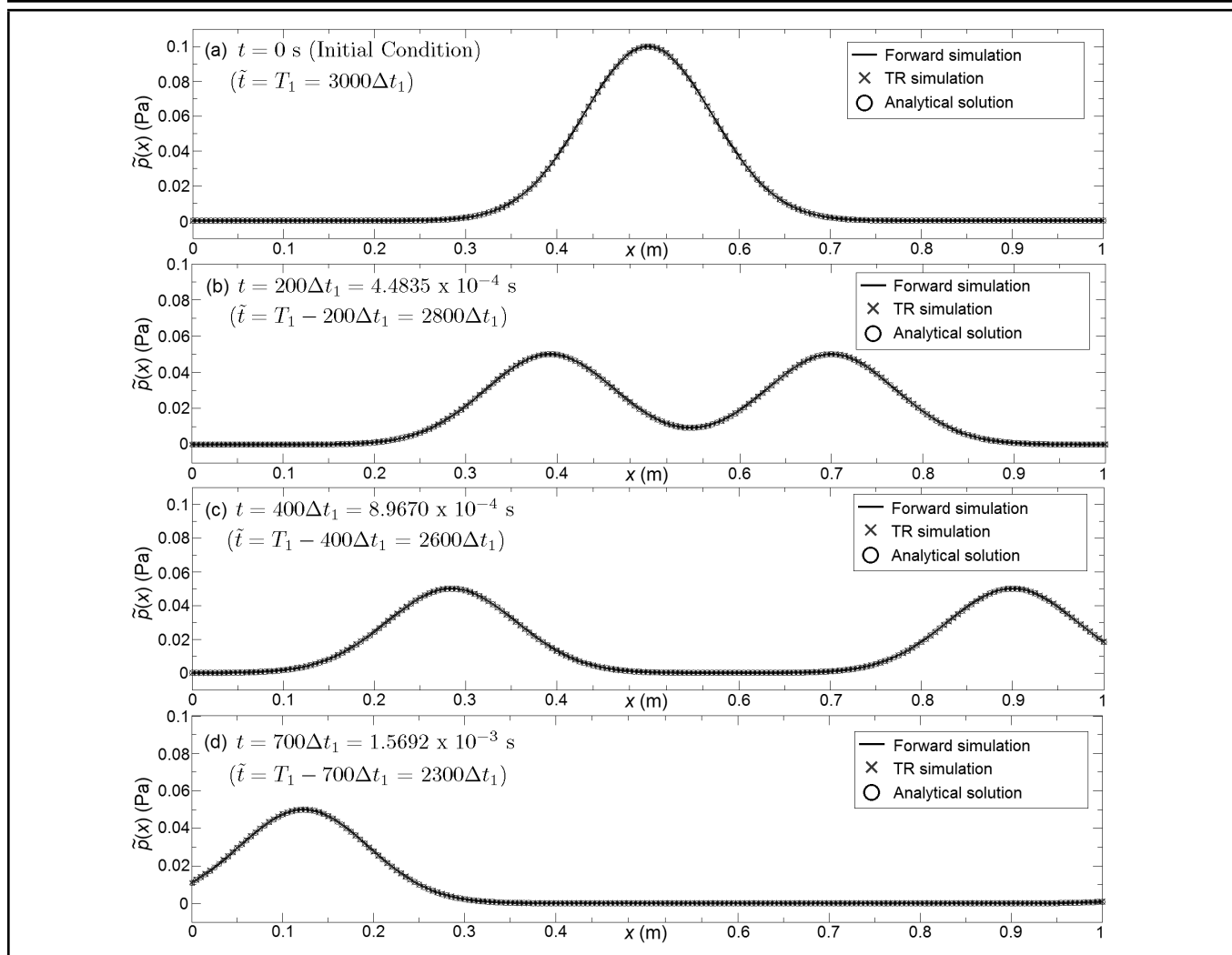
Figure 6. The acoustic pressure field $\tilde{p}(x,t)$ computed using the forward simulation of a Gaussian pulse propagating in a 1-D infinite duct (shown in Fig. 1(a)) with mean flow $M_0 = 0.3$ towards the positive x direction at time-instants $t =$ (a) 0, (b) $200\Delta t_1$, (c) $400\Delta t_1$, and (d) $700\Delta t_1$, and comparison with the analytical solution (given by Eq. (24)). The time-reversed acoustic pressure field $\tilde{p}(x,\tilde{t})$ obtained during the TR simulation using only the time-reversed acoustic pressure as input at the boundary nodes at the reverse time-instants $\tilde{t} =$ (a) $2300\Delta t_1$, (b) $2600\Delta t_1$, (c) $2800\Delta t_1$, and (d) $T_1 = 3000\Delta t_1$ demonstrates one-to-one correspondence with the forward simulation and the analytical solution.

is noted that analysing the L_1 norm errors is meaningful only over the time interval $\tilde{t} = [1500\Delta t, 3000\Delta t]$ corresponding to arrival of the acoustic pulses at the computational boundaries until the coalescing of the two pulses to form a single amplified acoustic pressure pulse at time $\tilde{t} = T_1$. The order of magnitude of L_1 norm errors is approximately 10^{-5} over the interval $\tilde{t} = [2000\Delta t, 3000\Delta t]$, whereas the order of magnitudes of $\tilde{p}(x,\tilde{t})$ and $\rho_0 c_0 \tilde{u}(x,\tilde{t})$ over the same time interval is approximately 10^{-2}, while the peak of the Gaussian pulse in $\tilde{p}(x = L/2, \tilde{t} = T_1)$ is of the order 10^{-1}. This confirms the accuracy of TR simulations using only the time-reversed acoustic pressure as input at the boundary nodes for the 1-D test case.

4.2. Test Case 2: Propagation of a Gaussian Pulse in a 2-D Free-space with Uniform Mean Flow

The initial acoustic pressure field $\phi(x,y)$ is taken as a 2-D Gaussian pulse given by $\tilde{p}(x,y,t=0) = \phi(x,y) = \varepsilon e^{-\alpha\{(x-x_0)^2 + (y-y_0)^2\}}$, where $\alpha = 100$ m^{-2}, $\varepsilon = 0.1$ Pa and $x_0 = y_0 = 0$ denotes its peak in the 2-D domain $|x| \leq (L_x + \Delta L_x)$, $|y| \leq (L_y + \Delta L_y)$, where $L_x = L_y = 0.5$ m,

while $N_{\text{sponge}} = 30$, therefore, $\Delta L_x = \Delta L_y = 30 \times 0.005$ m $= 0.15$ m. The maximum wavenumber content in the 2-D Gaussian pulse is determined by computing the Hankel transform of order zero[35] of the function $f(r) = e^{-\alpha r^2}$ and is given by $e^{-\frac{k_0^2}{4\alpha}}/(2\alpha)$. For the values of α considered, the maximum wavenumber content k_0 is less than 55 m^{-1}, thereby ensuring an accurate propagation of the pulse with the mesh-size considered here.

4.2.1. Forward Simulation

Figures 8(a–d) depict the spatio-temporal evolution of the Gaussian pulse in a 2-D free space (over the domain $|x| \leq 0.65$ m, $|y| \leq 0.65$ m) with a uniform mean flow $M_0 = 0.3$ considered along the positive x direction obtained by the forward simulation at time-instants (a) $t = 0$ (Initial condition), (b) $t = 300\Delta t_2$, (c) $t = 600\Delta t_2$, and (d) $t = 1000\Delta t_2$, where $\Delta t_2 = 2.2418 \times 10^{-6}$ s.

It is noted that the domain shown in Figs. 8(a–d) also includes the sponge-layer domain which is necessary to damp the incoming spurious reflections at the exterior computational boundaries. Furthermore, in Figs. 8(a–d), the direction of the uniform mean flow along the positive x direction is indicated
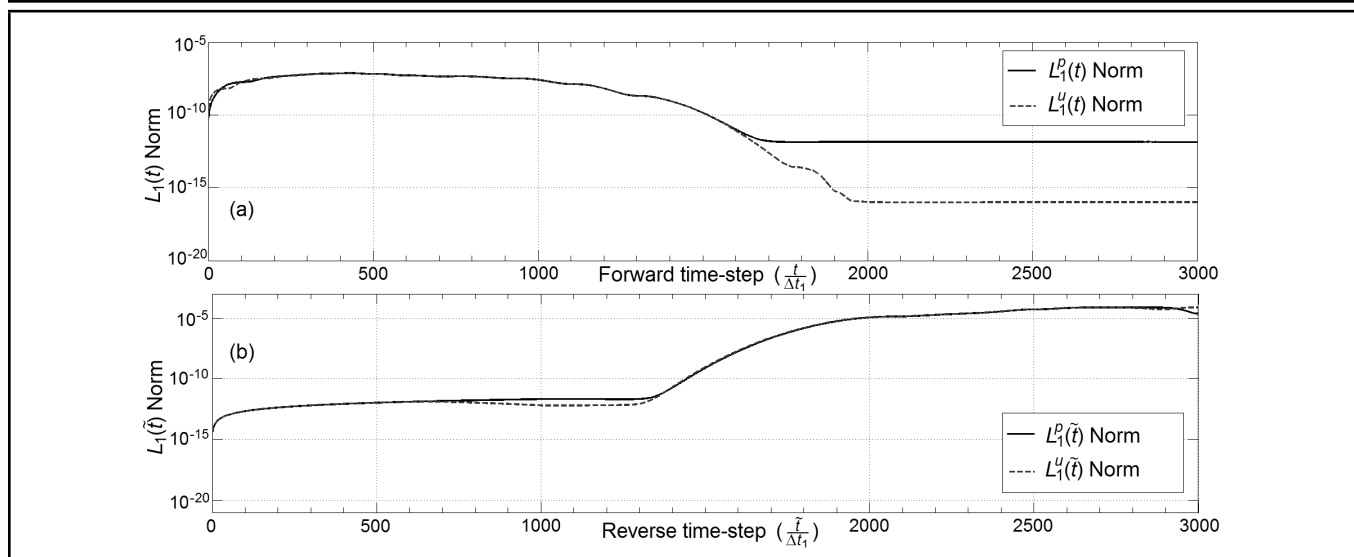
Figure 7. Temporal variation of (a) the $L_1(t)$ error norms in the 1-D forward simulation and (b) the $L_1(t)$ error norms in the 1-D TR simulation: Quantification of the accuracy of the simulations using the PCF of the LEE and the overall upwind-biased FD scheme.

by an arrow, the colorbar depicts the magnitude of acoustic pressure in Pa (Nm^{-2}), and the known location of the peak of the Gaussian pulse in Fig. 8(a) is indicated by a circle **O**. The same symbol and unit conventions are also followed for the remaining 2-D simulations. Figures 8(a–d) demonstrate that the 2-D Gaussian pulse collapses and the cylindrical wave fronts expand radially such that the center of pulse is convected with a speed $c_0 M_0$ towards positive x direction due to mean flow.

The accuracy of the 2-D forward simulation results (shown in Figs. 8(a–d)) is assessed by comparison against the corresponding analytical solution of the acoustic pressure field due to the spatio-temporally evolving Gaussian pulse in a 2-D free-space given by[16]

$$\tilde{p}(x, y, t) = \frac{\varepsilon}{2\alpha} \int\limits_{\xi=0}^{\xi=\xi_0 \to \infty} \xi e^{-\frac{\xi^2}{4\alpha}} \cos(c_0 \xi t) J_0(\xi \eta) \, d\xi; \quad (26)$$

where $J_0(\cdot)$ is the ordinary Bessel function of zero order and $\eta = \{(x - c_0 M_0 t)^2 + y^2\}^{1/2}$. Figures 9(a–d) depict the comparison of the acoustic pressure field $\tilde{p}(x, y = 0, t)$ along the x axis $t = [0, 300\Delta t_2, 600\Delta t_2, 1000\Delta t_2]$, respectively, obtained using forward simulation and the analytical solution, wherein an excellent agreement is observed between the two approaches, especially during the initial time-instants. At $t = 1000\Delta t_2$, the forward simulation results exhibit a small deviation from the analytical solution as may be observed from Fig. 9(d). It is however noted that the $\tilde{p}(x, y = 0)$ field predicted by the forward simulation and the corresponding analytical solution are both of the order 10^{-3}, while the discrepancy between the two approaches (due to small wave reflections that back propagate into the computational domain despite the use of Tam's ABC at the $x = 0.65$ m boundary and the use of sponge-layer near nodes of this boundary) is of the order of 10^{-4}. This indicates that a reasonable estimate of the $\tilde{p}(x, y, t)$ field may be obtained by means of forward simulations based on the PCF of 2-D LEE, overall upwind-biased FD schemes, and the implementation of ABC. Indeed, the forward simulations were carried out for $t = [0, 5000\Delta t_2]$ during which the Gaussian pulse completely propagates out of the 2-D domain,

and the acoustic pressure and particle velocity fields tend to zero.

The $\tilde{p}(x, y, t)$ field obtained using the overall central DRP FD scheme[16, 20] based on the PCF and implementation of ABC was found to be similar to that shown in Figs. 8(a–d), (the results are not shown for brevity), thereby demonstrating the stability and accuracy of the 2-D forward simulations using the overall central DRP FD scheme.

4.2.2. TR Simulation

Time-reversed Acoustic Pressure as Input

Figures 10(a–d) show the $\tilde{p}(x, y, \tilde{t})$ field predicted by the 2-D TR simulations (over the domain $|x| \leq 0.5$ m, $|y| \leq 0.5$ m,) using only the time-reversed acoustic pressure history as input at all four computational boundaries, i.e. $x = \pm 0.5$ m and $y = \pm 0.5$ m at (a) $\tilde{t} = 4000\Delta t_2$, (b) $\tilde{t} = 4400\Delta t_2$, (c) $\tilde{t} = 4700\Delta t_2$, and (d) $\tilde{t} = T_2 = 5000\Delta t_2$ (the final time-instant of TR simulation). The 'reversed' direction of mean flow is indicated by an arrow in Figs. 10(a–d), while the predicted location of the peak of the Gaussian pulse in Fig. 10(d) is indicated by a cross **X**. (These same symbolic conventions are also followed for the remaining results.) It is noted that the use of time-reversed acoustic pressure Dirichlet boundary conditions as input at the four computational boundaries results in the generation of both the incoming acoustic wave fronts (that propagates into the domain, converges and eventually coalesces to form the initial Gaussian pulse) and the outgoing waves that tend to propagate outside the computational domain. In order to prevent the spurious numerical reflections at the boundaries due to the outgoing waves from back-propagation into the domain and thereby inducing instability, the CEM ABC and the special corner ABCs were implemented at the boundaries,[4, 10, 21] crucial for stabilising the 2-D TR simulations. Furthermore, $\partial \tilde{v}/\partial x|_{x=L_x} = 0$ condition was also implemented to prevent instability due to incoming disturbances advected by 'reversed' mean flow.

Figure 10(d) indicates that the predicted location of the peak of the Gaussian pulse is co-incident with the known peak location. Indeed, a comparison of $\tilde{p}(x, y, \tilde{t})$ field in Figs. 10(a–d) with the corresponding $\tilde{p}(x, y, t)$ field shown in Figs. 8(d–
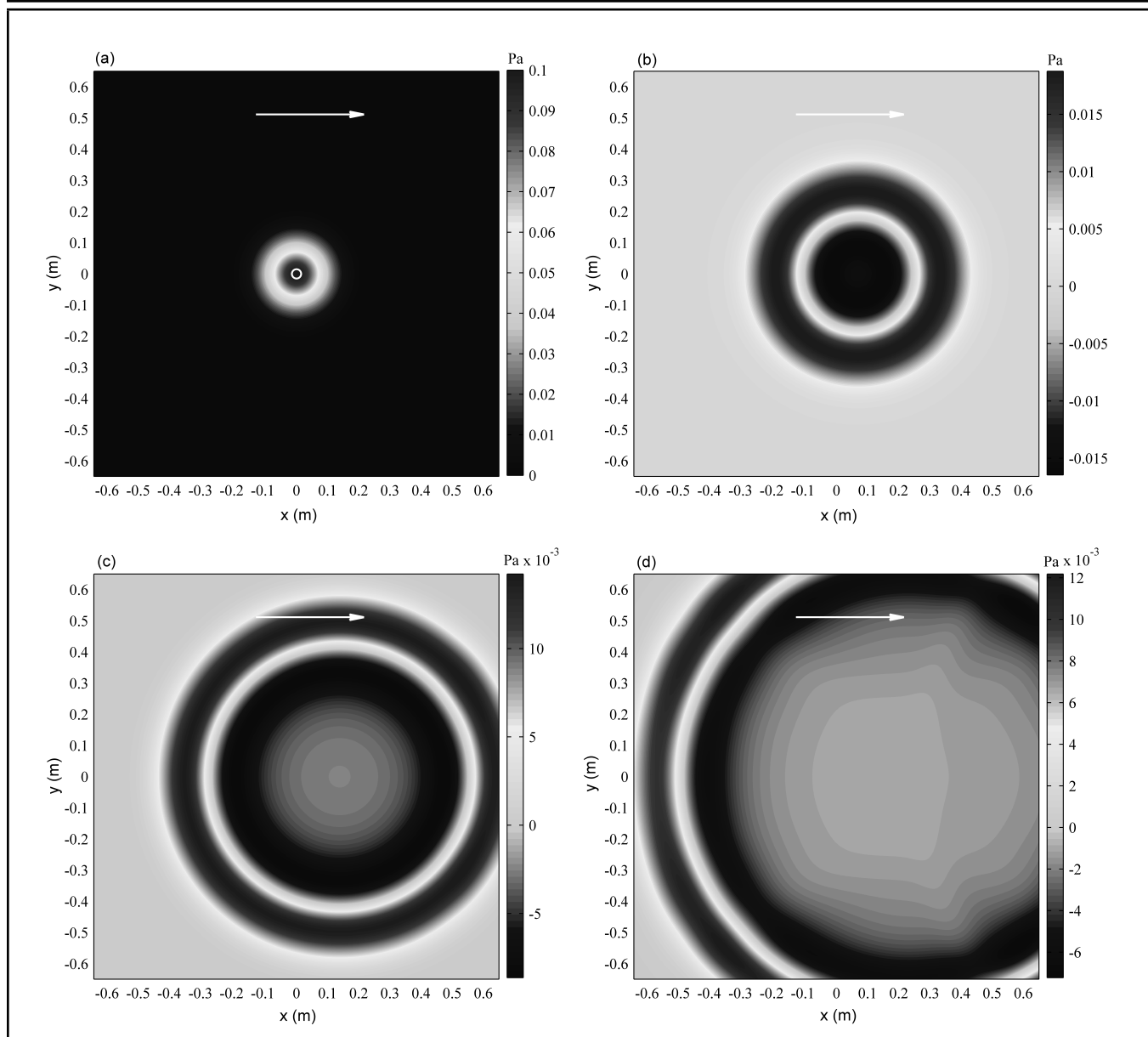
Figure 8. The forward simulation of acoustic pressure field $\tilde{p}(x, y, t)$ due to a Gaussian pulse propagating in a 2-D free-space with uniform mean flow $M_0 = 0.3$ towards the positive x direction at $t =$ (a) 0, (b) $300\Delta t_2$, (c) $600\Delta t_2$, and (d) $1000\Delta t_2$. It is noted that different colorbar scales are used in parts (a–d).

a), respectively, demonstrates an accurate back- propagation of cylindrical acoustic waves from the boundaries during 2-D TR simulations using only the time-reversed acoustic pressure as input. A similar conclusion may also be drawn on comparing the time-reversed $\tilde{p}(x, y = 0, \tilde{t})$ field with the forward $\tilde{p}(x, y = 0, t)$ field shown in Fig. 9.

Time-reversed Acoustic Pressure and Particle Velocities as Input: A Comparison

The $\tilde{p}(x, y, \tilde{t})$ field obtained by the 2-D TR simulations using both the time-reversed acoustic pressure and acoustic particle velocities as input (shown in Figs. 11(a–d)) is compared to that obtained using only the time-reversed acoustic pressure as input (shown in Figs. 10(a–d)) at the corresponding reverse time-instants.

It is observed that the $\tilde{p}(x, y, \tilde{t})$ fields obtained in Figs. 10(a–d) and 11(a–d) are similar. In particular, Figs. 10(d) and 11(d) predicting the initial location of peak of the Gaussian pulse are identical. Similar conclusions may also be made from

Figs. 9(a–d). This demonstrates that measuring the acoustic particle velocity histories at the computational boundaries is unnecessary and the use of only the time-reversed acoustic pressure as input is sufficient for an accurate localization of sound sources in flows by means of 2-D TR simulations.

It is also observed by means of numerical experiments that the use of an overall central DRP FD scheme[16, 20] for 2-D TR simulations using (a) only the time-reversed acoustic pressure as input, or (b) both the time-reversed acoustic pressure and acoustic particle velocities as input is unsuitable due to instability problems (despite implementing the ABC at the boundary nodes). This temporal instability is attributed to the identically zero damping in the central FD schemes. Hence, the unresolved spurious numerical waves generated at the computational boundaries due to implementation of Dirichlet boundary conditions[3] cannot be suppressed and thus propagate in the domain leading to instability.
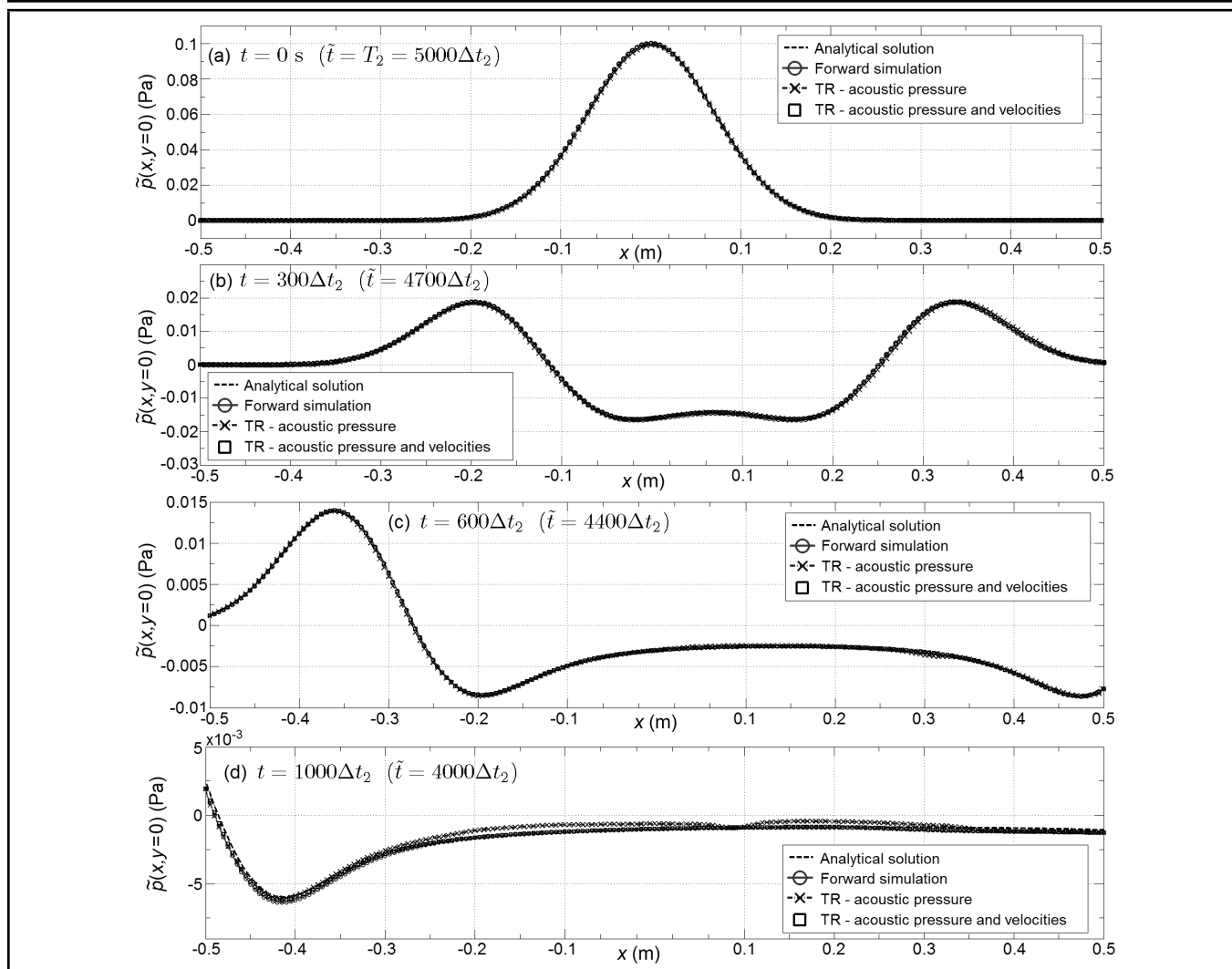
Figure 9. Spatio-temporal evolution of the acoustic pressure field along the x axis, i.e., $\tilde{p}(x, y = 0)$: Comparison of the analytical solution with results of the forward simulation, the TR simulation with only time-reversed acoustic pressure as input and TR simulation with both, the time-reversed acoustic pressure and particle velocity as input at the computational boundaries.

5. CONCLUSIONS

The temporal stability and accuracy of the forward and TR simulations of the Linearised Euler Equations (LEE) based on the Pseudo-Characteristic Formulation (PCF) and using two different classes of overall Finite-Difference (FD) schemes, (a) upwind-biased schemes and (b) central DRP schemes, have been analysed. The important contributions of this investigation are:

1. The stability of the 1-D forward and TR simulations using the overall upwind-biased FD scheme has been established by means of a matrix eigenvalue decomposition, wherein it is shown that two opposite upwinding directions must be considered for computing the spatial derivatives in the opposing fluxes of the PCF. The implementation of ABC is necessary to ensure stability of both, the 1-D and 2-D forward simulation of a pulse propagating in a free-space (with mean flow) over an arbitrarily large time duration. The stability of 1-D TR simulation using only time-reversed acoustic pressure as input is due to the use of upwind-biased schemes near the boundary and interior nodes, and the use of optimised downwind schemes at and near the boundary nodes having DRP property over a large range of wave numbers. Unlike the 1-D TR simulation, the ABC must be implemented for ensuring the stability of the 2-D TR simulation using overall upwind-biased schemes.

2. The stability of the forward simulation using the overall central DRP FD schemes[16, 20] in the PCF is also ensured by implementation of the ABC, wherein the execution time-step of the central DRP FD scheme is found to be almost half that of the overall upwind-biased FD scheme. However, for the 1-D TR simulations, some of the eigenvalues of overall central DRP FD schemes[16, 20] (without ASD[32]) are shown to have significantly large positive real parts, which implies the manifestation of instabilities towards the final time-instants. In fact, for the 2-D TR simulations, these instabilities manifest during the initial time-instants. Therefore, it may be concluded that the overall central DRP FD schemes are unsuitable for the TR simulation.

3. It is demonstrated that the use of both the time-reversed acoustic pressure and acoustic particle velocity histories as input during TR simulation is unnecessary. Rather, use of (a) only the time-reversed acoustic pressure his-
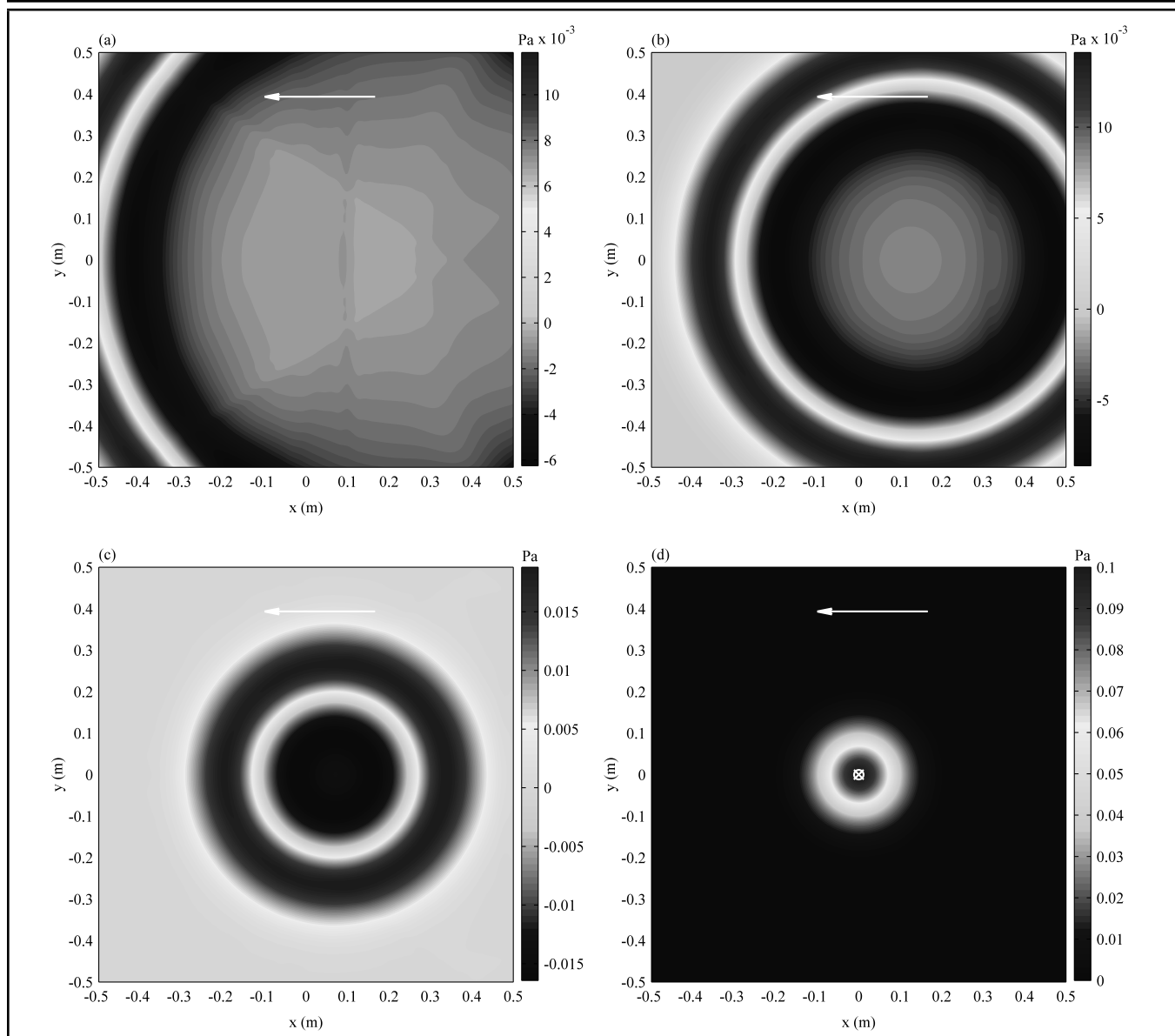
Figure 10. The acoustic pressure field $\tilde{p}(x, y, \tilde{t})$ due to back-propagation of a Gaussian pulse in a 2-D free-space obtained by means of the TR simulation using only the time-reversed acoustic pressure as input Dirichlet conditions at the nodes on the computational boundaries at reverse time-instants $\tilde{t} =$ (a) $4000\Delta t_2$, (b) $4400\Delta t_2$, (c) $4700\Delta t_2$, and (d) $T_2 = 5000\Delta t_2$. (The direction of uniform mean flow is reversed.)

tory as input at computational boundaries, and (b) the numerically reversed mean flow profile (which is known, a-priori during the forward simulation[4, 7, 10, 36] or experimentally measured using hot-wire anemometry[3]) is sufficient to warrant an accurate back-propagation of waves and thereby localise the sound source(s) in flow fields using the TR method.

4. The accuracy of the forward and TR simulation (using the overall upwind-biased FD schemes and PCF) is established by comparing the 1-D/2-D simulation results of the propagation of a Gaussian pulse in a free-space to the corresponding analytical solution. The physical significance of the accuracy analysis of TR simulation, in particular, is that for acoustic pressure and velocity fields at every forward time-instant t, there exists corresponding time-reversed acoustic pressure and velocity fields at reverse time $\tilde{t} = T - t$, thus, analytically validating the aeroacoustic TR simulation for the first time using simple test cases of back-propagation of a pulse in a free-space.

ACKNOWLEDGEMENTS

REFERENCES

[1] Fink, M. Time reversal of ultrasonic fields, I. Basic principles, *IEEE Transactions on Ultrasonics, Ferroelectrics, and Frequency Control*, **39** (5), 555–556, (1992).

[2] Fink, M., Cassereau, D., Derode, A., Prada, C., Roux, P., Tanter, M., Thomas, J. L., and Wu, F. Time-reversed acoustics, *Report on Progress in Physics*, **63** (12), 1933–1995, (2000).

[3] Padois, T., Prax, C., Valeau, V., and Marx, D. Experimental localization of an acoustic sound source in a wind-tunnel flow by using a numerical time-reversal technique, *Journal*
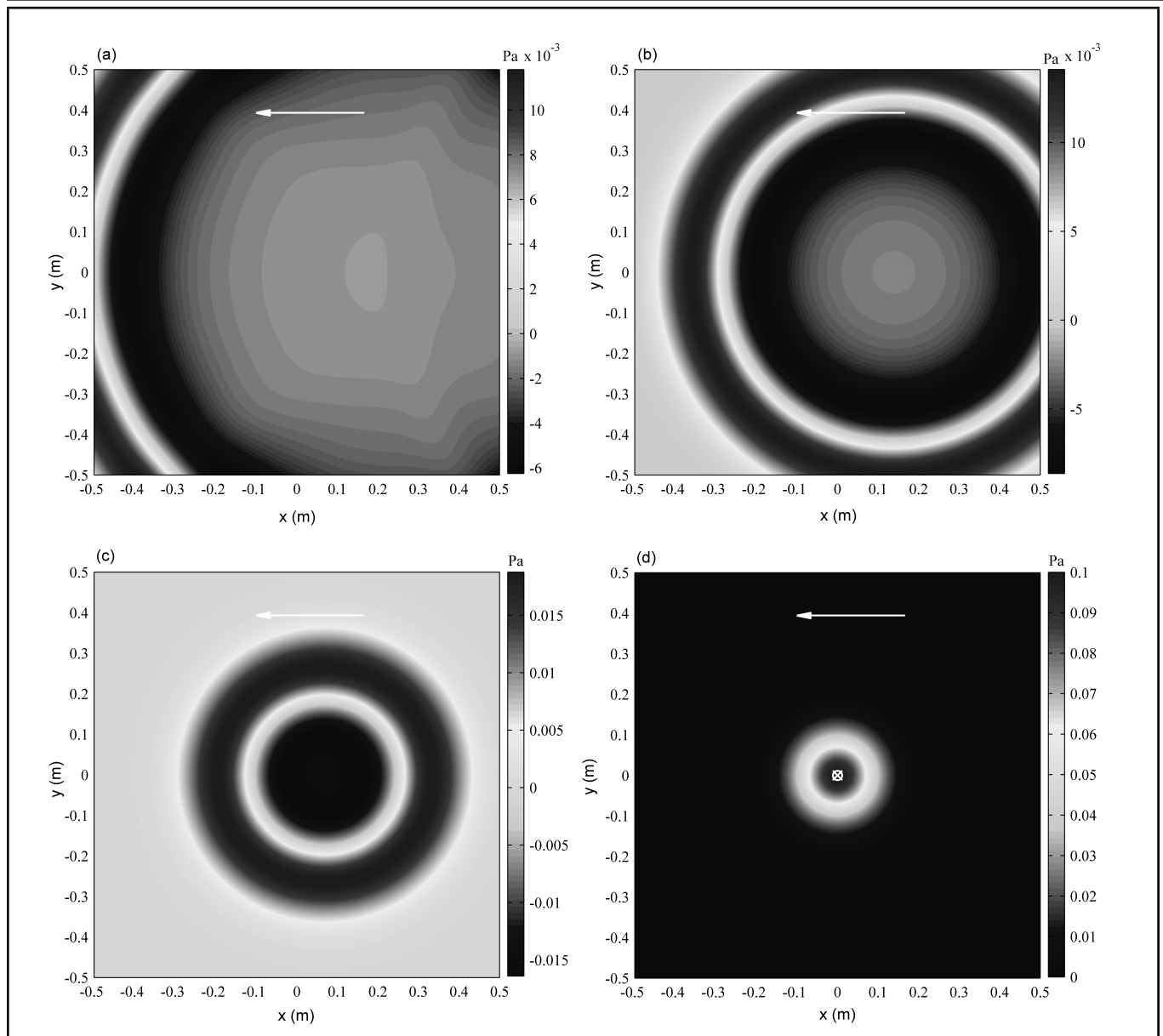
Figure 11. The acoustic pressure field $\tilde{p}(x, y, \tilde{t})$ due to back-propagation of a Gaussian pulse in a 2-D free-space obtained by means of the TR simulation using both, the time-reversed acoustic pressure and velocities as input Dirichlet conditions at the nodes on the computational boundaries at reverse time-instants $\tilde{t} =$ (a) $4000\Delta t_2$, (b) $4400\Delta t_2$, (c) $4700\Delta t_2$, and (d) $T_2 = 5000\Delta t_2$. (The direction of uniform mean flow is reversed.)

of the *Acoustical Society of America*, **132** (4), 2397–2407, (2012).

4 Mimani. A., Doolan, C. J., and Medwell, P. R. Multiple line arrays for the characterization of aeroacoustic sources using a time-reversal method, *Journal of the Acoustical Society of America*, **134** (4), EL327–EL333, (2013).

5 Shimura, T., Watanabe, Y., Ochi, H., and Song, H. C. Long-range time reversal communication in deep water: Experimental results, *Journal of the Acoustical Society of America*, **132** (1), EL49–EL53, (2012).

6 Park, H. W., Sohn, H., Law, K. H., and Farrar, C. R., Time reversal active sensing for health monitoring of a composite plate, *Journal of Sound and Vibration*, **302** (1–2), 50–66, (2007).

7 Mimani. A., Doolan, C. J., and Medwell, P. R. Aeroacoustic time-reversal in the presence of a reflecting surface, Paper

No. 96, *Proc. 43rd International Congress on Noise Control Engineering InterNoise 2014*, Melbourne, Australia, (2014).

8 Lerosey, G., Rosny, J. D., Tourin, A., Derode, A., Montaldo. G., and Fink, M. Time reversal of electromagnetic waves, *Physical Review Letters*, **92** (19), 193904, (2004).

9 Bavu, E., Besnainou, C., Gibiat, V., Rosny, J. D., and Fink, M. Subwavelength sound focusing using a time-reversal acoustic sink, *Acta Acustica United with Acustica*, **93** (5), 706–715, (2007).

10 Mimani. A., Doolan, C. J., and Medwell, P. R. Enhancing the focal-resolution of aeroacoustic time-reversal using a point sponge-layer damping technique, *Journal of the Acoustical Society of America*, **136** (3), EL199–EL205, (2014).

11 Deneuve, A., Druault, P., Marchiano, R., and Sagaut, P. A

coupled time-reversal/complex differentiation method for aeroacoustic sensitivity analysis: towards a source detection procedure, *Journal of Fluid Mechanics*, **642**, 181–212, (2010).

12 Sesterhenn, J. A characteristic-type formulation of the Navier-Stokes equations for high order upwind schemes, *Computers and Fluids*, **30** (1), 37–67, (2001).

13 Lu, S.-Y. and Sagaut, P. Pseudo-characteristic formulation and dynamic boundary conditions for computational aeroacoustics, *International Journal of Numerical Methods in Fluids*, **53** (2), 201–227, (2007).

14 Bailly, C. and Juve, D. Numerical solution of acoustic wave propagation problems using linearized Euler equations, *AIAA Journal*, **38** (1), 22–29, (2000).

15 Zhang, R., Qin, G., and Zhu, C. Spectral element method for acoustic propagation problems based on linearized Euler equations, *Journal of Computational Acoustics*, **17** (4), 383–402, (2009).

16 Tam, C. K. W. and Webb, J. C., Dispersion-relation-preserving finite-difference schemes for computational acoustics, *Journal of Computational Physics*, **107** (2), 262–281, (1993).

17 Toro, E. F. *Riemann Solvers and Numerical Methods for Fluid Dynamics*, Springer-Verlag, Berlin, (1999), 2ⁿᵈ Edition, 265–291.

18 Sesterhenn, J., Muller, B., and Thomann, H., Flux-Vector Splitting for compressible low mach number flow, *Computers and Fluids*, **22** (4), 441–451, (1993).

19 Lele, S. K. Compact finite difference schemes with spectral-like resolution, *Journal of Computational Physics*, **103** (1), 16–42, (1992).

20 Tam, C. K. W. Computational aeroacoustics: issues and methods, *AIAA Journal*, **33** (10), 1788–1796, (1995).

21 Mimani, A. and Moreau, D. J. and Prime, Z. and Doolan, C. J., Enhanced focal-resolution of dipole sources using aeroacoustic time-reversal in a wind-tunnel, Mechanical Systems and Signal Processing. (2015), DOI: 10.1016/j.ymssp.2015.09.037.

22 Zhuang, M. and Chen, R. F. Applications of high-order optimised upwind schemes for computational aeroacoustics, *AIAA Journal*, **40** (3), 443–449, (2002).

23 Li, Y. Wavenumber-extended high-order upwind-biased finite-difference schemes for convective scalar transport, *Journal of Computational Physics*, **133** (2), 235–255, (1997).

24 Berland, J., Bogey, C., Marsden, O., and Bailly, C., High-order, low dispersive and low dissipative explicit schemes for multiple-scale and boundary problems, *Journal of Computational Physics*, **224** (2), 637–662, (2007).

25 Gottlieb, S. and Shu, C.-W. Total variation diminishing Runge-Kutta schemes, *Mathematics of Computation*, **67** (221), 73–85, (1998).

26 Clayton, R. and Engquist, B. Absorbing boundary conditions for acoustic and elastic wave equations, *Bulletin of the Seismological Society of America*, **67** (6), 1529–1540, (1977).

27 Engquist, B. and Majda, A. Absorbing boundary conditions for the numerical simulation of waves, *Mathematics of Computation*, **31** (139), 629–651, (1977).

28 Engquist, B. and Majda, A. Radiation boundary conditions for acoustic and elastic wave calculations, *Communications in Pure and Applied Mathematics*, **32** (3), 313–357, (1979).

29 Strang, G. *Linear algebra and its applications*, Thomson Brooks/Cole, (2005), 3ʳᵈ Edition, 275–286.

30 Shukla, R. K., Tatineni, M., and Zhong, X. Very high-order compact finite difference schemes on non-uniform grids for incompressible Navier Stokes equations, *Journal of Computational Physics*, **224** (2), 1064–1094, (2007).

31 Marburg, S. Normal modes in external acoustics. Part I: Investigation of the one-dimensional duct problem, *Acta Acustica United with Acustica*, **91** (6), 1063–1078, (2005).

32 Tam, C. K. W, Webb, J. C., and Dong, Z. A study of the short wave components in computational acoustics, *Journal of Computational Acoustics*, **1** (1), 1–30, (1993).

33 Lockard, D. P., Brentner, K. S., and Atkins, H. L. High-accuracy algorithms for computational aeroacoustics, *AIAA Journal*, **33** (2), 246–251, (1995).

34 Tam, C. K. W. *Computational aeroacoustics: A wave number approach*, Cambridge University Press, New York, (2012), 30–36.

35 Myint-U, T. and Debnath, L. *Linear partial differential equations for scientists and engineers*, Birkhäuser Boston, (2007), 4ᵗʰ Edition, 488–495, 691–694.

36 Mimani, A., Prime, Z., Doolan, C. J., and Medwell, P. R. A sponge-layer damping technique for aeroacoustic time-reversal, *Journal of Sound and Vibration* **342**(1), 124–151, (2015).